

VLBI astrometry of radio stars to link radio and optical celestial reference frames - II. 11 radio stars

Jingdong Zhang,^{1,2,3} Bo Zhang,^{1*} Shuangjing Xu,^{4,1} Xiaofeng Mai,^{1,2,5} Mark J. Reid,⁶ Pengfei Jiang,⁷ Wen Chen,^{8,9} Fengchun Shu,¹ Jinling Li,¹ Lang Cui,⁷ Xingwu Zheng,¹⁰ Yan Sun,¹ and Zhaoxiang Qi^{1,2}

¹Shanghai Astronomical Observatory, Chinese Academy of Sciences, 80 Nandan Road, Shanghai 200030, People's Republic of China

²University of Chinese Academy of Sciences, No.19 (A) Yuquan Rd, Shijingshan, Beijing 100049, People's Republic of China

³Department of Geodesy and Geodynamics, Finnish Geospatial Research Institute (FGI), National Land Survey of Finland, Vuorimiehentie 5, Espoo 02150, Finland

⁴Korea Astronomy and Space Science Institute, 776 Daedeok-daero, Yuseong-gu, Daejeon 34055, Republic of Korea

⁵University of Helsinki, P.O. Box 64, FI-00014, Finland

⁶Harvard-Smithsonian Center for Astrophysics, 60 Garden Street, Cambridge, MA 02138, USA

⁷Xinjiang Astronomical Observatory, Chinese Academy of Sciences, 150 Science 1-Street, Urumqi 830011, People's Republic of China

⁸Yunnan Observatories, Chinese Academy of Sciences, Kunming 650216, Yunnan, People's Republic of China

⁹Yunnan Key Laboratory of the Solar Physics and Space Science, Kunming 650216, People's Republic of China

¹⁰School of Astronomy and Space Science, Key Laboratory of Modern Astronomy and Astrophysics (Ministry of Education), Nanjing University, Nanjing 210023, People's Republic of China

Accepted XXX. Received YYY; in original form ZZZ

ABSTRACT

The alignment between the radio-based International Celestial Reference Frame (ICRF) and the optical *Gaia* Celestial Reference Frame (*Gaia*-CRF) is critical for multi-waveband astronomy, yet systematic offsets at the optical bright end ($G \lesssim 13$) limit their consistency. While radio stars offer a potential link between these frames, their utility has been restricted by the scarcity of precise Very Long Baseline Interferometry (VLBI) astrometry. In this study, we present new VLBI astrometry of 11 radio stars using the Very Long Baseline Array (VLBA), expanding the existing sample with positions, parallaxes, and proper motions measured. All 11 radio stars were detected, for 10 of which parallaxes and proper motions can be estimated, achieving median uncertainties better than 0.1 mas and 0.1 mas yr⁻¹, respectively. These new samples greatly contribute to the link between ICRF and *Gaia*-CRF at the optical bright end.

Key words: radio continuum: stars – astrometry – parallaxes – proper motions – reference systems

1 INTRODUCTION

The establishment of a unified celestial reference frame (CRF) covering all bands is critical for advancing multi-waveband astronomy, geodesy, and deep-space navigation. At radio wavelengths, the International Celestial Reference Frame (ICRF, Ma et al. 1998) is the radio realization of the International Celestial Reference System (ICRS, Arias et al. 1995) and is defined through Very Long Baseline Interferometry (VLBI) observations of extragalactic sources (quasars). Its latest iteration, ICRF3, achieved a coordinate noise floor of 30 μ as (Charlot et al. 2020). In the optical band, the third data release of the *Gaia* mission (*Gaia* DR3, Gaia Collaboration et al. 2023) provides astrometry for over 1.6 million quasars, defining the optical realization of the ICRS, the *Gaia* Celestial Reference Frame 3 (*Gaia*-CRF3), which has comparable precision to ICRF3 (Gaia Collaboration et al. 2022).

Gaia-CRF3 is aligned to ICRF3 at a 7 μ as level (formal uncertainty) using common quasars (Gaia Collaboration et al. 2022). However, systematic discrepancies persist for optical bright sources

($G \lesssim 13$) in *Gaia* DR3, attributed to magnitude-, color-, and galactic-latitude-dependent shifts in centroid determinations and instrument calibration limitations, such as the Window Class (WC) effects (Lindgren 2020). These systematics manifest as orientation offsets and residual spins between the bright *Gaia*-CRF3 and the quasar-based ICRF3 (Lindgren et al. 2018; Brandt 2018), necessitating independent validation to achieve an accurate and stable alignment between the CRFs.

Given the optical faintness of most quasars, efforts to link the frames rely on radio stars, which are observable in both radio and optical (bright-end) bands (Malkin 2016). Several studies have attempted to align *Gaia*-CRF to ICRF with radio stars, e.g., Lindgren (2020); Bobylev (2022); Lunz et al. (2023, 2024); Zhang et al. (2024). However, the small number of available radio stars restricts the robustness of the alignment: positions and proper motions of only several tens of radio stars have been measured with VLBI.

It is also possible to assess the bright *Gaia*-CRF internally within *Gaia*, which is not restricted by sample numbers. For example, Cantat-Gaudin & Brandt (2021) estimated spin parameters with samples collected from known binaries and open clusters. However, orientation parameters cannot be estimated through this method.

* E-mail: zb@shao.ac.cn

It is therefore crucial to increase the number of radio stars with VLBI measurements; to this end, we have undertaken observations within the framework of a long-term research initiative. Observing strategies for radio star astrometry with VLBI are discussed in [Zhang et al. \(2024\)](#). Our pilot Very Long Baseline Array (VLBA) program (obs. ID: BZ077) successfully measured parallaxes and proper motion of two radio stars, HD 199178 and AR Lac ([Chen et al. 2023](#)). In another program (VLBA obs. ID: BZ080), we observed three radio stars: HD 179094, RZ Cas, and SZ Psc ([Jiang et al. in prep.](#)). This study presents new VLBI astrometry for 11 radio stars, focusing on the data reduction and astrometric results, while the frame link results with all the new data are presented in [Zhang et al. \(2025c\)](#).

The paper is organized as follows: Sect. 2 describes the VLBI observations; Sect. 3 details the data reduction; Astrometric results are presented in Sect. 4; Finally we summarize in Sect. 5.

2 OBSERVATIONS

Our observations were conducted under VLBA programs BZ087, BZ103, and BZ107. The target selection is introduced in Sect. 2.1, while the observation setups and scheduling are introduced in Sect. 2.2 and 2.3, respectively.

2.1 Target selection

We selected target radio stars from the Very Large Array (VLA) historical observations. For example, 46 radio stars were observed with the Very Large Array Plus Pie Town ([Boboltz et al. 2007](#)). These stars are detectable on baselines of tens of kilometers; however, it is in doubt whether they are bright enough to be detected on baselines of thousands of kilometers. Therefore, we confirmed through snapshot observation whether they can be detected with VLBI. The snapshot was conducted under the European VLBI Network (EVN) program EZ029 at X band, with 11 antennas (Wb, Ef, Mc, O6, T6, Ur, Ys, Ir, Sv, Zc, Bd), recording rate of 1 Gbps, and on-source time of about five minutes for each star. Six stars (HD 199178, IM Peg, SZ Psc, RZ Cas, RS CVn, and V1762 Cyg) were detected with an SNR > 5, in which three (HD 199178, SZ Psc, and RZ Cas) were observed in previous programs (obs. ID: BZ077 and BZ080), and one was selected to be observed in this program (RS CVn).

The Very Large Array Sky Survey (VLASS, [Gordon et al. 2021](#)) provides a great number of candidates for VLBI observation. Through crossmatching the VLASS catalog with the SIMBAD ([Wenger et al. 2000](#)) database and *Gaia* DR2 ([Gaia Collaboration et al. 2018](#)), we selected 73 radio star candidates that are point-like and have a brightness of > 1 mJy/beam. Then we confirmed their detectability through another snapshot observation (EVN obs. ID: EX009) at C band. A recording rate of 2 Gbps, and an on-source time of about ten minutes for each star were adopted, providing twice the sensitivity as EZ029. 20 candidates were detected, and we selected ten to be observed in this program. Information of all 11 selected stars is listed in Table 1, which all have no parallax and proper motion measured with VLBI before. The stars are divided into five groups according to their right ascension for easier scheduling.

10 of the 11 selected stars are binaries except for V1859 Ori, with orbital periods ranging from 0.5 to 21 days ([Eker et al. 2008](#)). A reliable estimation of the binary orbits requires an unaffordable amount of observing time for the ten binaries. Fortunately, the angular scales of the binary orbits are one to two orders of magnitude smaller than the value of their parallaxes and proper motions.

2.2 Observation setups

Most radio stars are weak at radio frequencies (about millijansky level), so we requested the maximum capability of VLBA to achieve a high sensitivity: all 10 antennas, a recording rate of 4 Gbps, dual polarization, and 2-bit quantization. The radiation of radio stars that we can detect mainly has a non-thermal nature, and their fluxes decrease as the frequency increases at centimeter wavelengths ([Wilson et al. 2013](#)), so C band (~ 5 GHz) is a good balance between flux and angular resolution. Ionospheric propagation delay at C band is also smaller than at lower frequencies. On the other hand, the C-band receiver provides the lowest System Equivalent Flux Density (SEFD), i.e., the highest sensitivity, among all VLBA receivers¹.

For weak sources, including radio stars, phase referencing (PR, [Lestrade et al. 1990](#); [Beasley & Conway 1995](#)) using a nearby known calibrator enables precise differential astrometry. However, atmospheric spatial structures can introduce additional propagation delays due to the angular separation between the calibrator and the target. To achieve better atmospheric spatial structure correction compared to single-calibrator PR (hereafter referred to simply as PR) and thereby improve astrometric precision, the MultiView technique ([Rioja et al. 2017](#)) is used: multiple calibrators that enclose the target are cyclically observed, allowing for a linear phase gradient estimation on the sky plane and interpolation at the target position. The C band is suitable for the application of MultiView, e.g., [Hyland et al. \(2023\)](#).

Each target is surrounded by four calibrators, selected from the ICRF3 catalog ([Charlot et al. 2020](#)) and the Radio Fundamental Catalog (RFC, [Petrov & Kovalev 2025](#), rfc_2024d used in this work)², which are listed in Table 2. The calibrators are categorized into two types: primary calibrators and secondary calibrators. The primary calibrators serve as absolute position references, meaning the phases of secondary calibrators are residual phases relative to them during the MultiView procedure, which is further introduced in Sect. 3.1. As the primary calibrators are all collected from the ICRF3 catalogue, the absolute positions of the targets we measure are in the ICRF3 system. See Appendix B of [Zhang et al. \(2025b\)](#) for more details about the absolute positioning.

The observing sequence is “C1-C2-T-C3-C4”, where “C*n*” and “T” denote the *n*th calibrator and the target, respectively. The observing cycle is ~200 seconds, typically including 50 seconds on the target and about 20 to 30 seconds on each calibrator according to their fluxes. An example of the observing cycle for FF UMa is shown in Fig. 1, whose total cycle length is 209 seconds.

2.3 Scheduling

Due to the typically low and variable fluxes of radio stars, seven epochs were scheduled for each group of targets to improve the likelihood of successfully measuring their parallaxes and proper motions. The epochs span a period of three years, from 2021 to 2025, instead of the usual one year: BZ087 in semester 2021B, BZ103 in 2024A, and BZ107 in 2024B. This improves the accuracy of proper motions, the most important parameter for CRF spin estimation. The epochs are optimized to sample near the extremes of parallax sinusoids to enable more accurate parallax measurements ([Reid 2022](#)). The actual epochs for each session are listed in Table 3.

For the groups comprising two radio stars (groups A, B, C, and E), 5 hours are allocated per epoch, whereas for the group including

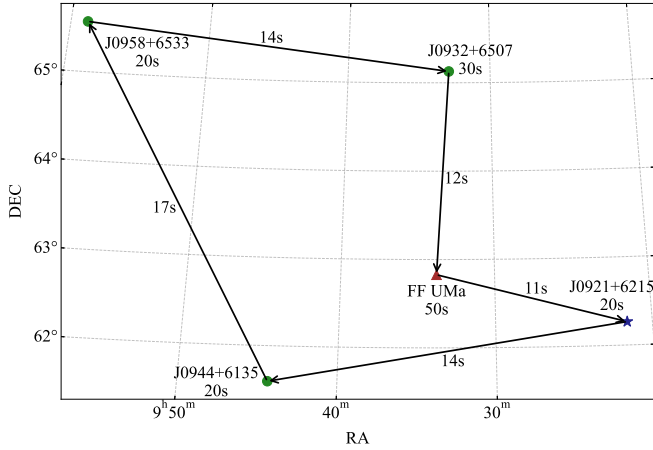
¹ <https://science.nrao.edu/facilities/vlba/docs/manuals/oss/bands-perf>

² <https://doi.org/10.25966/dhrk-zh08>

Table 1. Optical information of selected radio stars

Group	Name	Type	RA (J2000) (h m s)	DEC (J2000) (° ′ ″)	σ_{α^*} (mas)	σ_{δ} (mas)	ϖ (mas)	μ_{α^*} (mas yr ⁻¹)	μ_{δ} (mas yr ⁻¹)	G (mag)	RUWE
A	FF Aqr HD 8357	EB	22:00:36.4256	-02:44:26.869	0.030	0.030	4.734±0.034	31.284±0.037	-10.173±0.035	9.1	2.1
		XB	01:22:56.7569	+07:25:09.332	0.038	0.028	21.981±0.045	94.296±0.048	231.124±0.034	7.1	1.6
B	EI Eri V1859 Ori	RS CVn	04:09:40.8924	-07:53:34.176	0.030	0.022	18.380±0.039	37.847±0.039	102.570±0.032	7.0	1.9
		T Tau	05:22:54.7927	+08:58:04.679	0.014	0.011	3.480±0.016	1.375±0.016	-9.264±0.012	9.9	1.1
C	V1355 Ori AR Mon	RS CVn	06:02:40.3604	-00:51:37.225	0.018	0.016	7.842±0.023	11.859±0.024	11.693±0.020	8.9	1.2
		RS CVn	07:20:48.4543	-05:15:35.797	0.021	0.022	2.298±0.027	7.154±0.029	-6.763±0.028	8.4	1.2
D	XY UMa	RS CVn	09:09:55.9355	+54:29:17.724	0.010	0.010	14.722±0.014	-49.781±0.012	-182.641±0.012	9.4	1.0
	FF UMa	RS CVn	09:33:46.5476	+62:49:40.254	0.015	0.019	8.620±0.027	-20.220±0.019	-22.002±0.027	7.6	1.5
	DM UMa	RS CVn	10:55:43.5438	+60:28:09.721	0.011	0.011	5.386±0.016	-37.912±0.014	-7.566±0.014	8.9	1.2
E	RS CVn	RS CVn	13:10:36.9078	+35:56:05.585	0.013	0.013	7.349±0.023	-49.898±0.012	20.754±0.019	7.8	1.1
	RS UMi	RS CVn	15:50:49.4329	+72:12:40.628	0.011	0.011	2.119±0.011	3.392±0.013	-8.534±0.014	9.9	1.0

In the column “Type”, “EB” and “XB” denote Eclipsing Binary and X-ray Binary, respectively. Astrometric parameters are from *Gaia* DR3. σ_{α^*} and σ_{δ} denote position errors in the RA ($\alpha \cos \delta$) and DEC directions, respectively. Column “ G ” gives *Gaia* G -band magnitude. RUWE denotes *Gaia* Renormalized Unit Weight Error.


Figure 1. The MultiView observing cycle for FF UMa.

three stars (group D), the observing time is 6.5 hours. This ensures an on-source time of about 40 minutes for each radio star, and the corresponding theoretical thermal noise is $\sim 20 \mu\text{Jy}/\text{beam}$.

3 DATA REDUCTION

3.1 Calibration

The raw data were correlated by the VLBA DiFX software correlator (Deller et al. 2007) in Socorro. A preliminary calibration with standard PR workflow using the primary calibrator was applied to the visibility data:

(i) Amplitude calibration with the Astronomical Image Processing System (AIPS, Greisen 2003) tasks ACCOR and APCAL, where the former automatically corrects amplitudes in cross-correlation spectra and the latter corrects based on system temperature and gain curve tables.

(ii) Parallax angle and Earth Orientation Parameters (EOP) correction with the AIPS task CLCOR.

(iii) Ionospheric Faraday rotation and dispersive delay correction with the AIPS task TECOR based on the global ionosphere maps provided by the Jet Propulsion Laboratory (JPL).

(iv) Manual phase calibration with the AIPS task FRING, i.e., fringe fitting with a fringe finder to remove electronic phase differences among different intermediate frequency (IF) bands.

(v) Fringe fitting (FRING) with the primary calibrator and apply the result to the target and all secondary calibrators.

Most of the non-spatial systematic errors were removed through the PR procedure above. Then serial MultiView (sMV, Zhang et al. 2025b) was applied to remove the residual spatial-structure errors. The sMV is an implementation of the MultiView techniques that enables automatic phase ambiguity correction. In order to include the time-domain information and detect “phase wrap” robustly, the sMV operates on the time series of calibrator scans, rather than fitting independent linear phase gradients to each scan group as done in the conventional MultiView implementation. Fringe fitting with the secondary calibrators separately yields their residual phases relative to the primary calibrator, since the fringe fitting result with the primary calibrator has already been applied to them. Under the assumption that the residual phases change continuously, the phase plane should be highly predictable over a short time range, enabling ambiguity detection. The phase plane is iteratively rotated to follow the changes in the residual phase time series, and then the phase correction to be applied to the target can be interpolated in the space and time domain.

We developed a pipeline based on AIPS and ParselTongue (Ketenis et al. 2006), and it is used for all data in this study. For the data used in this work (with the observing sequence “C1-C2-T-C3-C4”), the calibration performance of the sMV pipeline shows virtually no difference from the conventional MultiView implementation, which has been verified in Zhang et al. (2025b). Details of the whole procedure can also be found there.

After calibration, the targets were mapped and cleaned with the AIPS task IMAGR. An image example is shown in Appendix A. All targets in this study are point-like sources, so their positions were fitted with the AIPS task JMFIT, assuming a single 2-D Gaussian component for each target. All measured positions are available in Appendix B.

Table 2. Calibrators selected for each radio star

Target	Calibrator	RA (J2000) (^h ^m ^s)	DEC (J2000) ([°] ['] ^{''})	σ_{α^*} (mas)	σ_{δ} (mas)	S_{unres} (Jy)	Dist. ([°])
FF Aqr	J2156-0333	21:56:50.156791	-03:33:27.94729	0.16	0.32	0.051 (X)	1.25
	J2156-0037★	21:56:14.757927	-00:37:04.59451	0.07	0.13	0.548 (X)	2.39
	J2206-0031	22:06:43.282610	-00:31:02.49526	0.10	0.19	0.138 (C)	2.70
	J2204-0616	22:04:44.681846	-06:16:03.38787	0.22	0.46	0.087 (X)	3.67
HD 8357	J0119+0829	01:19:01.274274	+08:29:54.70398	0.16	0.38	0.217 (C)	1.45
	J0130+0842	01:30:27.634426	+08:42:46.17184	0.09	0.18	0.192 (X)	2.27
	J0121+0422★	01:21:56.861693	+04:22:24.73429	0.03	0.03	0.664 (C)	3.06
	J0121+1149	01:21:41.595041	+11:49:50.41323	0.03	0.03	1.564 (C)	4.42
EI Eri	J0408-0749 [†]	04:08:45.373699	-07:49:36.07436	0.75	1.73	0.139 (C)	0.24
	J0408-0529★	04:08:59.649940	-05:29:40.53842	0.10	0.22	0.213 (X)	2.40
	J0357-0751	03:57:43.293242	-07:51:14.56748	0.09	0.21	0.113 (X)	2.96
	J0422-0643	04:22:10.795426	-06:43:45.33073	0.10	0.22	0.204 (X)	3.31
V1859 Ori	J0519+0848	05:19:10.811132	+08:48:56.73464	0.08	0.16	0.283 (X)	0.93
	J0517+0648★	05:17:51.344133	+06:48:03.21075	0.13	0.22	0.085 (X)	2.50
	J0532+0732	05:32:38.998475	+07:32:43.34559	0.53	0.53	0.071 (C)	2.80
	J0521+1227 [†]	05:21:59.770901	+12:27:05.55162	0.24	0.48	0.202 (C)	3.49
V1355 Ori	J0558-0055	05:58:44.391585	-00:55:06.92915	0.30	0.49	0.106 (X)	0.98
	J0606-0024★	06:06:57.443582	-00:24:57.46389	0.13	0.30	0.102 (C)	1.16
	J0615-0119 [†]	06:15:40.214886	-01:19:04.66677	0.20	0.47	0.141 (C)	3.28
	J0613-0008 [†]	06:13:35.914480	-00:08:33.74424	0.12	0.26	0.179 (C)	2.82
AR Mon	J0724-0715★	07:24:17.292627	-07:15:20.35241	0.06	0.13	1.409 (X)	2.18
	J0728-0453 [†]	07:28:48.213248	-04:53:47.77855	0.16	0.28	0.147 (C)	2.02
	J0709-0255	07:09:45.054609	-02:55:17.49663	0.08	0.15	0.270 (X)	3.62
	J0730-0241	07:30:25.877613	-02:41:24.90444	0.08	0.17	0.330 (X)	3.52
XY UMa	J0902+5402	09:02:19.287489	+54:02:57.25641	0.13	0.15	0.135 (C)	1.19
	J0903+5151★	09:03:58.574560	+51:51:00.66298	0.11	0.12	0.174 (C)	2.78
	J0854+5757	08:54:41.996416	+57:57:29.93913	0.05	0.06	0.671 (C)	4.06
	J0927+5717	09:27:06.053451	+57:17:45.34313	0.18	0.22	0.089 (C)	3.70
FF UMa	J0921+6215★	09:21:36.231076	+62:15:52.18035	0.03	0.03	0.588 (C)	1.51
	J0944+6135 [†]	09:44:20.441650	+61:35:50.19380	0.10	0.15	0.105 (C)	1.74
	J0932+6507	09:32:54.577582	+65:07:41.29670	0.13	0.13	0.137 (X)	2.30
	J0958+6533	09:58:47.245113	+65:33:54.81804	0.03	0.03	1.276 (C)	3.86
DM UMa	J1048+6008 [†]	10:48:33.699074	+60:08:45.64158	0.20	0.23	0.041 (C)	0.94
	J1104+6038★	11:04:53.694641	+60:38:55.31456	0.13	0.15	0.099 (C)	1.14
	J1102+5941	11:02:42.762830	+59:41:19.58467	0.13	0.15	0.164 (C)	1.17
	J1101+6241	11:01:53.450783	+62:41:50.60470	0.22	0.28	0.220 (C)	2.35
RS CVn	J1308+3546★	13:08:23.709135	+35:46:37.16400	0.03	0.04	0.370 (C)	0.48
	J1317+3425	13:17:36.494184	+34:25:15.93242	0.05	0.07	0.232 (C)	2.08
	J1310+3233	13:10:59.402733	+32:33:34.44955	0.03	0.03	0.592 (C)	3.38
	J1317+3925 [†]	13:17:18.635659	+39:25:28.14246	0.16	0.21	0.092 (C)	3.73
RS UMi	J1531+7206★	15:31:33.578594	+72:06:41.22799	0.11	0.09	0.215 (X)	1.48
	J1556+7420	15:56:02.990517	+74:20:58.14090	0.11	0.13	0.104 (C)	2.17
	J1603+6945	16:03:18.621508	+69:45:57.44291	0.16	0.14	0.073 (X)	2.65
	J1646+7419 [†]	16:46:15.172466	+74:19:11.06490	0.30	0.34	0.025 (X)	4.5

The calibrators with “★” are used as the primary calibrator for sMV and the calibrator for PR. Most positions and uncertainties in this table are from the ICRF3 catalog, while those sources not included in ICRF3 are labeled with “[†]”, and their positions and uncertainties are collected from `rffc_2024d`. Column “ σ_{α^*} ” and “ σ_{δ} ” denote position uncertainties in the RA ($\alpha \cos \delta$) and DEC directions respectively. Unresolved fluxes, along with their corresponding bands in parentheses, are collected from `rffc_2024d` and listed in column “ S_{unres} ”. Column “Dist.” denotes angular distance from the target.

Table 3. Observing epochs for each group

Group	Semester (program code)								
	2021B (BZ087)			2024A (BZ103)			2024B (BZ107)		
A	2021-11-20	2021-12-26	-	2024-06-03	2024-06-14	2024-07-03	2024-11-30	2025-01-23	
B	2021-08-19	2021-09-11	2022-01-16	2024-03-04	2024-04-03	-	2024-08-16	2024-10-07	
C	2021-09-05	2021-10-21	-	2024-03-02	2024-03-27	2024-05-04	2024-09-15	2024-10-30	
D	2021-10-09	2021-12-06	-	2024-04-14	2024-05-05	2024-06-04	2024-10-18	2024-12-07	
E	2021-08-10	2021-08-18	2021-12-13	2024-02-09	2024-03-13	-	2024-08-19	2024-09-05	

The date format is YYYY-MM-DD.

3.2 Astrometric parameter estimation

For stars with ≥ 3 detections, position at reference epoch, parallax, and proper motion can be estimated. Here we adopt an astrometric model of five parameters: $[\alpha, \delta, \varpi, \mu_{\alpha*}, \mu_{\delta}]$. Binary orbit, Galactocentric acceleration, and other possible small terms are not taken into consideration. For the parallactic motion, the DE440 (Park et al. 2021) ephemeris provided by JPL was used to calculate precise coordinates of the Earth in the Barycentric System. The emcee Markov Chain Monte Carlo sampler (Foreman-Mackey et al. 2013) was used for parameter estimation.

Usually, errors in VLBI astrometry consist of both thermal and systematic errors (Reid 2022). The AIPS task JMFIT calculates a theoretical uncertainty based on the image root mean square (RMS), leading to a significant underestimation of systematic errors. Therefore, systematic error floors in the RA and DEC directions are iteratively added during astrometric parameter estimation to achieve a reduced chi-square $\chi_{\text{red}}^2 \approx 1$. Note this can only be done for stars with ≥ 4 detections because the iteration procedure requires an extra degree of freedom in each direction.

As discussed in Sect. 2.1, the angular scales of the orbits of the binaries are small. Therefore, a single-star model is used for fitting. And on the other hand, binaries with such short periods and small orbital scales are also fitted with single-star models in the current *Gaia* astrometric solution; as discussed in Halbwachs et al. (2023), the shortest astrometric binary period (~ 30 days) successfully solved in *Gaia* DR3 is larger than the longest one (AR Mon, 21 days) in our targets.

3.3 Details of each star

In general, the data quality is high, with the vast majority of calibrators being sufficiently bright and compact. The detection rate for targets reaches $\sim 82\%$, typically appearing as point-like sources, and the sMV gives higher SNRs than PR in most cases. Multiple antennas were experiencing rainfall during the sessions in which sMV does not perform well. Special cases and non-detections will be introduced below.

FF Aqr

FF Aqr has a slightly variable flux (the measured values for the point-like radio stars are the peak flux density S_{peak} , same below). There is one epoch (BZ103A2) where sMV gives a lower SNR than PR. One of the calibrators, J2156-0333, shows a slight jet-like structure, but it does not introduce significant spurious phases into the residual phase time series. Here, “spurious phase” refers to an evident phase inconsistency between this calibrator and the others on some or all baselines (same definition used below). Self-calibrated images of

J2156-0333 and other calibrators with notable structures are shown in Appendix E.

HD 8357

The flux of HD 8357 is highly variable, varying from about 0.2 mJy to over 20 mJy. There is one epoch (BZ087A2) where sMV gives a lower SNR than PR. One of the calibrators, J0119+0829, has complex structures and shows significant spurious phases, so it is not used for sMV phase plane estimation.

EI Eri

The flux of EI Eri is highly variable, varying from about 0.5 mJy to over 30 mJy.

V1859 Ori

The flux of V1859 Ori is highly variable, varying from about 0.2 mJy to about 5 mJy. One of the calibrators, J0532+0732, is not compact enough, so it does not contribute much to the long baselines (fringe fitting failure or being flagged).

V1355 Ori

V1355 Ori was not detected in one epoch (BZ087C1), and its flux is highly variable, varying from about 0.3 mJy to about 5 mJy.

AR Mon

AR Mon was only detected in the first two epochs (BZ087C1, BZ087C2), which is not enough for astrometric parameter estimation.

XY UMa

XY UMa was only detected in three epochs (BZ087D1, BZ087D2, and BZ103D2), which is enough for astrometric parameter estimation but not enough for the iterative systematic error estimation procedure (insufficient degrees of freedom, as discussed in Sect. 3.2). There is one epoch (BZ087D2) where sMV gives a lower SNR than PR.

FF UMa

The flux of FF UMa is highly variable, varying from about 1 mJy to over 20 mJy.

DM UMa

DM UMa was not detected in the last epoch (BZ107D2), and its flux is slightly variable in the first 6 epochs. DM UMa is the only case that sMV gives lower SNRs than PR in all epochs. Two of the secondary calibrators, J1048+6008 and J1102+5941, have jet-like structures that cause significant spurious phases. Both of the remaining two calibrators are on the same side of DM UMa, making it impossible to interpolate phases at the position of DM UMa without J1048+6008 and J1102+5941.

RS CVn

RS CVn was not detected in one epoch (BZ087E3), and its flux is highly variable, varying from about 0.4 mJy to about 4 mJy. There are two epochs (BZ087E1, BZ107E2) where sMV gives lower SNRs than PR, and the SNRs are very close: this is due to the very small angular separation (0.48°) between the primary calibrator and the target.

RS UMi

RS UMi was not detected in two epochs (BZ087E2, BZ103E1), and its flux is highly variable, varying from about 0.3 mJy to about 2 mJy. There are two epochs (BZ087E1, BZ107E2) where sMV gives lower SNRs than PR. One of the calibrators, J1646+7419, has complex structures and shows significant spurious phases, so it is not used for sMV phase plane estimation.

4 RESULTS

4.1 Gains of MultiView

The MultiView techniques should outperform PR in ideal situations, that is, there are close enough calibrators enclosing the target, the calibrators are compact and have precise a priori positions, the observing cycle is within the coherence time, and most importantly, the atmosphere (and/or other spatial-structure errors) is the dominant error source.

The performance comparison between the sMV and PR can be conducted using the RMS-based JMFIT error or the fractional flux recovery (FFR) quantity, which is defined as the ratio between the peak brightness in the astrometric image and the self-calibrated image of the same source (Rioja et al. 2017). The radio stars are too weak for self-calibration, so here we use the ratio between the peak flux densities of PR and sMV instead.

Fig. 2 shows the JMFIT error ratio of PR to sMV versus the RA and DEC offsets between the target and the primary calibrator of all sessions. The sMV in most cases (99/126) reduces the errors ($\text{PR}/\text{sMV} > 1$), and it is worth noting that in cases where sMV performs poorly, DM UMa accounts for about half of them (12/27). Another star with poor sMV performance is RS UMi, which, as mentioned in Sect. 3.3, lost an available calibrator.

Fig. 3 shows the peak flux density ratio of sMV to PR versus the angular separation between the target and the primary calibrator. Similar to the JMFIT error, the sMV reduces flux loss in most cases ($\text{sMV}/\text{PR} > 1$, 50/63), and the poor cases are mainly attributed to DM UMa and RS UMi (9/13).

The performance advantage of the sMV over PR is positively correlated with the angular separation between the target and the primary calibrator, especially in the DEC direction, as shown in Fig. 2 and 3. This is reasonable since observations are usually conducted around

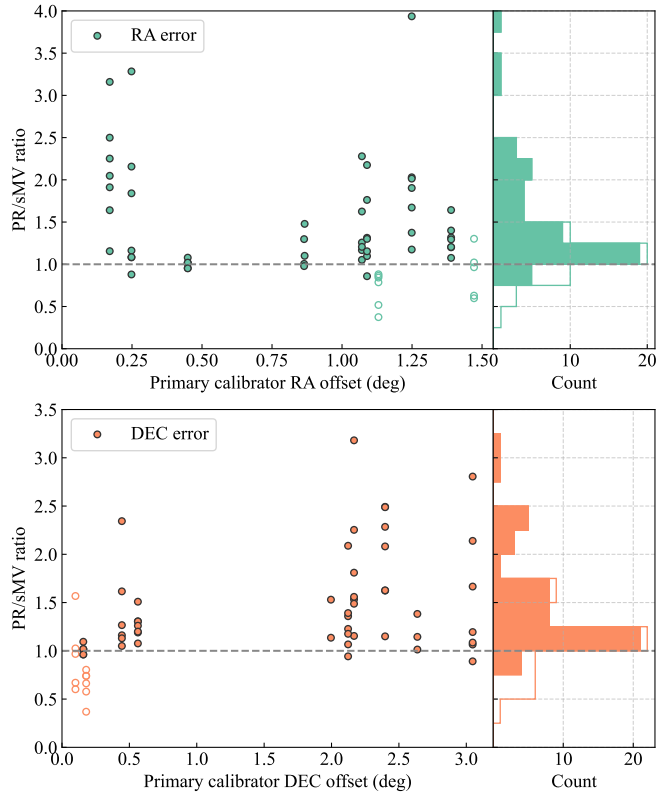


Figure 2. JMFIT error ratio of PR to sMV versus the RA and DEC offsets between the target and the primary calibrator (which also serves as the PR calibrator). The histogram is shown on the right side. Upper panel: RA direction; Lower panel: DEC direction. RA offsets are multiplied by $\cos \delta$ of the targets. Hollow markers in the scatterplots and hollow areas in the histograms denote data points of DM UMa and RS UMi.

its transit, and angular separations in the DEC direction correspond to differences in elevation angle. Residual delays/phases from both the ionosphere and troposphere tend to be more pronounced in the vertical direction than in the horizontal direction, especially at low elevation angles.

4.2 Astrometric parameters

The estimated astrometric parameters for ten stars (excluding AR Mon) are listed in Table 4, and the corresponding parallax curves are presented in Appendix C. The position uncertainties of primary calibrators are added to the position uncertainties of targets, so that the uncertainties reflect errors in absolute position rather than offsets to primary calibrators. As discussed in Sect. 3.3, the uncertainties for astrometric parameters of XY UMa are unreliable.

The performance advantage of sMV over PR is related to the angular separation between the target and the primary calibrator. For stars with a primary calibrator located within $\sim 1.5^\circ$ (V1355 Ori, FF UMa, RS CVn, RS UMi), the sMV and PR uncertainties are at the same level. While for the other stars, the sMV shows a significant advantage over PR, with two exceptions, HD 8357 and DM UMa.

HD 8357 has a relatively large angular scale of its binary orbit. The semimajor axis projected on the radial direction of its active component $a \sin i = 4.9 \times 10^6$ km, where a is the semimajor axis and i is the inclination (Fekel 1996). Calculating with its *Gaia* parallax $\varpi = 21.981$ mas, the corresponding maximum angular orbital offset

Table 4. Estimated astrometric parameters for ten stars

Star	Tech.	RA (h m s)	DEC (° ′ ″)	σ_{α^*} (mas)	σ_{δ} (mas)	ϖ (mas)	μ_{α^*} (mas yr ⁻¹)	μ_{δ} (mas yr ⁻¹)
FF Aqr	PR	22:00:36.4739537	-02:44:27.109490	0.176	0.338	4.308±0.131	32.740±0.083	-11.740±0.138
	sMV★	22:00:36.4739751	-02:44:27.109979	0.126	0.212	4.564±0.072	32.774±0.043	-11.826±0.061
HD 8357	PR	01:22:56.9041797	+07:25:14.704807	0.341	0.676	22.968±0.350	93.811±0.228	230.943±0.464
	sMV★	01:22:56.9041707	+07:25:14.704379	0.351	0.738	22.638±0.366	93.885±0.223	230.683±0.483
EI Eri	PR	04:09:40.9526202	-07:53:31.732253	0.298	0.654	17.727±0.229	36.296±0.145	111.943±0.316
	sMV★	04:09:40.9526282	-07:53:31.731358	0.229	0.374	17.894±0.146	36.433±0.097	111.925±0.109
V1859 Ori	PR	05:22:54.7949086	+08:58:04.464105	0.227	0.466	3.478±0.101	1.130±0.067	-9.423±0.185
	sMV★	05:22:54.7948822	+08:58:04.463601	0.208	0.270	3.545±0.085	1.242±0.056	-9.372±0.034
V1355 Ori	PR	06:02:40.3788864	-00:51:36.953470	0.169	0.369	7.930±0.038	12.484±0.033	11.516±0.056
	sMV★	06:02:40.3788999	-00:51:36.953609	0.161	0.374	7.955±0.031	12.514±0.028	11.400±0.061
XY UMa	PR	09:09:55.8027021	+54:29:13.477616	0.245	0.443	14.865±0.345	-49.749±0.262	-182.950±0.236
	sMV★	09:09:55.8026472	+54:29:13.477129	0.399	0.662	14.729±0.571	-49.789±0.427	-182.889±0.328
FF UMa	PR	09:33:46.4791756	+62:49:39.738112	0.107	0.150	8.432±0.079	-20.065±0.059	-22.223±0.086
	sMV★	09:33:46.4791651	+62:49:39.738521	0.128	0.130	8.470±0.098	-20.057±0.073	-22.157±0.072
DM UMa	PR★	10:55:43.4245688	+60:28:09.544893	0.184	0.213	5.473±0.075	-37.848±0.050	-7.598±0.054
	sMV	10:55:43.4244712	+60:28:09.543163	0.272	0.446	5.473±0.207	-37.759±0.131	-7.186±0.236
RS CVn	PR	13:10:36.8122560	+35:56:06.066910	0.065	0.221	7.504±0.059	-49.952±0.026	20.552±0.134
	sMV★	13:10:36.8122478	+35:56:06.066804	0.097	0.181	7.488±0.104	-49.973±0.051	20.643±0.107
RS UMi	PR	15:50:49.4501630	+72:12:40.428824	0.151	0.193	2.208±0.049	3.291±0.034	-8.513±0.083
	sMV★	15:50:49.4500275	+72:12:40.428941	0.127	0.327	2.187±0.014	3.340±0.017	-8.684±0.180

The reference epoch is J2023.25. Column “Tech.” denotes calibration technique, PR or sMV. The calibration technique with “★” is adopted as the final astrometric result for each star. Correlation coefficient matrices of the adopted results are listed in Appendix D.

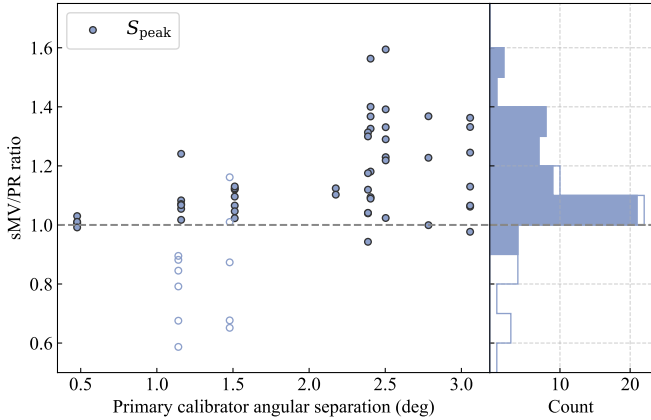


Figure 3. Peak flux density ratio of sMV to PR versus the angular separation between the target and the primary calibrator. The histogram is shown on the right side. Hollow markers in the scatterplot and hollow areas in the histogram denote data points of DM UMa and RS UMi.

would be no less than 0.72 mas, which is non-negligible. Therefore, unless a binary model is adopted, it is difficult to achieve further improvements at the current level of accuracy.

As mentioned in Sect. 3.3, only two available calibrators are available for DM UMa, and they are both located on the same side of DM UMa in the sky, which leads to a MultiView failure. Therefore, we adopt the PR result as the final astrometric result for DM UMa, whereas the sMV results are adopted for all other stars.

Overall, a high precision is achieved in most adopted astrometric results. Take parallaxes as an example, the mean parallax uncertainty is 0.156 mas, while the median is 0.091 mas. Parallax is a parameter that is not strongly affected by the systematic bright *Gaia*-CRF rotation, so a direct comparison between VLBI and *Gaia* is possible. Fig. 4 shows the comparison between the results and *Gaia* DR3 par-

allaxes, for which the zero-point issue has been corrected using the recipe and coefficients provided by Lindegren et al. (2021) and Ding et al. (2024), respectively.

Define the normalized residual between VLBI and *Gaia* parallaxes as

$$Z_{\varpi} = \frac{\varpi_{\text{VLBI}} - \varpi_{\text{Gaia}}}{\sqrt{\sigma_{\varpi_{\text{VLBI}}}^2 + \sigma_{\varpi_{\text{Gaia}}}^2}}, \quad (1)$$

and its absolute value $|Z_{\varpi}|$ can be calculated for each star, as shown in Table 5, together with other error statistics. We compared the normalized residuals with and without *Gaia* parallax zero-point correction, and the correction only reduces the mean absolute value of normalized residual by ~ 0.2 ($\langle |Z_{\varpi}| \rangle = 1.847$, $\langle |Z_{\varpi}^{\text{corr}}| \rangle = 1.639$). Assuming that the VLBI and *Gaia* measurements are independent, that their uncertainties are reasonable estimates, and that no additional systematic errors exist, Z_{ϖ} should follow a standard Gaussian distribution $\mathcal{N}(0, 1)$. Therefore, the probability that $|Z_{\varpi}| < 2$ is 95%. However, only six of the ten stars have $|Z_{\varpi}| < 2$, suggesting that one or both of VLBI and *Gaia* may have underestimated their uncertainties, or there exist systematic errors.

Due to the geometry of the VLBA network and the declinations of the targets, the restored synthesis beams for most targets are ellipses with approximately north-south-oriented long axes. As a result, the angular resolution in the DEC direction is not as good as that in the RA direction, and the uncertainties of the positions and proper motions in the DEC direction are worse.

5 SUMMARY

We observed 11 radio stars with the VLBA at C band. With 7 epochs spanning over 3 years, all 11 stars were detected at least twice. The data were calibrated using our pipeline with two techniques: single-calibrator phase referencing and serial MultiView. We successfully derived parallaxes and proper motions for 10 of them, achieving

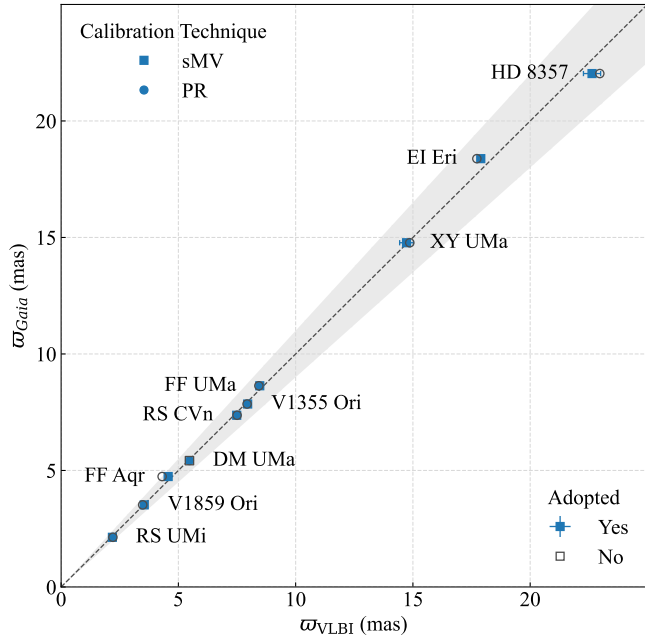


Figure 4. Comparison between the VLBI and *Gaia* parallaxes. Square and circle markers denote sMV and PR, respectively. Filled markers denote adopted results, and error bars are plotted for them. The reference dashed line has a slope of 1 and an intercept of 0. The filled area indicates a deviation range within $\pm 10\%$.

Table 5. Error statistics of the adopted parallaxes and proper motions

Star	$\sigma_{\varpi_{\text{VLBI}}}$ (mas)	$\sigma_{\mu_{\alpha^* \text{VLBI}}}$ (mas yr $^{-1}$)	$\sigma_{\mu_{\delta \text{VLBI}}}$ (mas yr $^{-1}$)	$ Z_{\varpi} $	$ Z_{\varpi}^{\text{corr}} $
FF Aqr	0.072	0.043	0.061	2.144	2.212
HD 8357	0.366	0.223	0.483	1.782	1.638
EI Eri	0.146	0.097	0.109	3.213	3.229
V1859 Ori	0.085	0.056	0.034	0.803	0.240
V1355 Ori	0.031	0.028	0.061	2.910	2.646
XY UMa	0.571	0.427	0.328	0.011	0.078
FF UMa	0.098	0.073	0.072	1.471	1.619
DM UMa	0.075	0.050	0.054	1.134	0.664
RS CVn	0.104	0.051	0.107	1.300	1.099
RS UMi	0.014	0.017	0.180	3.696	2.961
Mean	0.156	0.106	0.149	1.847	1.639
Median	0.091	0.053	0.089	1.627	1.628

Columns 2–4 list the uncertainties of the adopted parallaxes and proper motions. Column $|Z_{\varpi}|$ denotes the absolute value of the normalized residual between VLBI and *Gaia* DR3 parallaxes, while $|Z_{\varpi}^{\text{corr}}|$ is the normalized residual for *Gaia* DR3 parallaxes after zero-point correction.

median uncertainties better than 0.1 mas and 0.1 mas yr $^{-1}$, respectively. The high-quality data produced in this study are an important addition to the available radio star sample for the bright *Gaia*-CRF validation, and the frame link results are presented in Zhang et al. (2025c).

ACKNOWLEDGEMENTS

This work is supported by the Strategic Priority Research Program of the Chinese Academy of Sciences, Grant No. XDA0350205, the

National Natural Science Foundation of China (NSFC) under grant No. U2031212, and the National Key R&D Program of China (No. 2024YFA1611501). J. Zhang is supported by the Postdoctoral Programme for Research Institutes in Finland funded by the Finnish Government. W. Chen is supported by Yunnan Fundamental Research Projects (grant No. 202401AT070144) and Yunnan Foreign Talent Introduction Program (grant No. 202505AO120021).

The Python pipeline used for calibration can be found at the Astrophysics Source Code Library (Zhang et al. 2025a), and a “frozen” version used in this paper is available at Zenodo (Zhang 2025a). The Python program used for astrometric parameter estimation can be found at https://github.com/FrdCHK/mcmc_ppm_estimate, and a “frozen” version used in this paper is available at Zenodo (Zhang 2025b).

The RFC can be accessed through <https://doi.org/10.25966/dhrk-zh08>. This work has also made use of the SIMBAD database, operated at CDS, Strasbourg, France (Wenger et al. 2000, <https://simbad.u-strasbg.fr/simbad/>).

The European VLBI Network is a joint facility of independent European, African, Asian, and North American radio astronomy institutes. Scientific results from data presented in this publication are derived from the following EVN project codes: EZ029, EX009.

This work has made use of data from the European Space Agency (ESA) mission *Gaia* (<https://www.cosmos.esa.int/gaia>), processed by the *Gaia* Data Processing and Analysis Consortium (DPAC, <https://www.cosmos.esa.int/web/gaia/dpac/consortium>). Funding for the DPAC has been provided by national institutions, in particular the institutions participating in the *Gaia* Multilateral Agreement. The *Gaia* services (<https://gaia.ari.uni-heidelberg.de/index.html>) provided by the Astronomisches Rechen-Institut (ARI) of the University of Heidelberg are used in *Gaia* data retrieval. The Python package for *Gaia* DR3 parallax zero-point correction developed by P. Ramos can be found at https://gitlab.com/icc-ub/public/gaiadr3_zeropoint, and the coefficients used in this paper can be found at <https://github.com/yedings/Parallax-bias-correction-in-the-Galactic-plane>.

This research has made use of the Astrophysics Data System, funded by NASA under Cooperative Agreement 80NSSC21M0056.

Software and Python packages used in this work (in alphabetical order): AIPS (Greisen 2003), Astropy (Astropy Collaboration et al. 2013, 2018, 2022), Difmap (Shepherd 1997), emcee (Foreman-Mackey et al. 2013), Matplotlib (Hunter 2007), Numpy (Harris et al. 2020), Pandas (The pandas development Team 2024), ParselTongue (Kettenis et al. 2006), Scipy (Virtanen et al. 2020), and TOPCAT (Taylor 2005).

DATA AVAILABILITY

The EVN data used in this study can be downloaded from <https://archive.jive.nl/scripts/portal.php>. The VLBA data used in this study can be downloaded from the data archive of the National Radio Astronomy Observatory (NRAO; <https://data.nrao.edu>). VLBI images and parallax curves are available at Zenodo (Zhang 2025c): <https://doi.org/10.5281/zenodo.17348486>.

REFERENCES

- Arias E. F., Charlot P., Feissel M., Lestrade J.-F., 1995, *A&A*, **303**, 604
 Astropy Collaboration et al., 2013, *A&A*, **558**, A33
 Astropy Collaboration et al., 2018, *AJ*, **156**, 123

Astropy Collaboration et al., 2022, *ApJ*, **935**, 167

Beasley A. J., Conway J. E., 1995, in Zensus J. A., Diamond P. J., Napier P. J., eds, *Astronomical Society of the Pacific Conference Series Vol. 82, Very Long Baseline Interferometry and the VLBA*. p. 327

Boboltz D. A., Fey A. L., Puatua W. K., Zacharias N., Claussen M. J., Johnston K. J., Gaume R. A., 2007, *AJ*, **133**, 906

Bobylev V. V., 2022, *Astronomy Letters*, **48**, 790

Brandt T. D., 2018, *ApJS*, **239**, 31

Cantat-Gaudin T., Brandt T. D., 2021, *A&A*, **649**, A124

Charlot P., et al., 2020, *A&A*, **644**, A159

Chen W., et al., 2023, *MNRAS*, **524**, 5357

Deller A. T., Tingay S. J., Bailes M., West C., 2007, *PASP*, **119**, 318

Ding Y., Liao S., Wu Q., Qi Z., Tang Z., 2024, *A&A*, **691**, A81

Eker Z., et al., 2008, *MNRAS*, **389**, 1722

Fekel F. C., 1996, *AJ*, **112**, 269

Foreman-Mackey D., Hogg D. W., Lang D., Goodman J., 2013, *PASP*, **125**, 306

Gaia Collaboration et al., 2018, *A&A*, **616**, A1

Gaia Collaboration et al., 2022, *A&A*, **667**, A148

Gaia Collaboration et al., 2023, *A&A*, **674**, A1

Gordon Y. A., et al., 2021, *ApJS*, **255**, 30

Greisen E. W., 2003, in Heck A., ed., *Astrophysics and Space Science Library Vol. 285, Information Handling in Astronomy - Historical Vistas*. p. 109, doi:10.1007/0-306-48080-8_7

Halbwachs J.-L., et al., 2023, *A&A*, **674**, A9

Harris C. R., et al., 2020, *Nature*, **585**, 357

Hunter J. D., 2007, *Computing in Science and Engineering*, **9**, 90

Hyland L. J., et al., 2023, *ApJ*, **953**, 21

Kettenis M., van Langevelde H. J., Reynolds C., Cotton B., 2006, in Gabriel C., Arviset C., Ponz D., Enrique S., eds, *Astronomical Society of the Pacific Conference Series Vol. 351, Astronomical Data Analysis Software and Systems XV*. p. 497

Lestrade J. F., Rogers A. E. E., Whitney A. R., Niell A. E., Phillips R. B., Preston R. A., 1990, *AJ*, **99**, 1663

Lindgren L., 2020, *A&A*, **633**, A1

Lindgren L., et al., 2018, *A&A*, **616**, A2

Lindgren L., et al., 2021, *A&A*, **649**, A4

Lunz S., Anderson J. M., Xu M. H., Titov O., Heinkelmann R., Johnson M. C., Schuh H., 2023, *A&A*, **676**, A11

Lunz S., et al., 2024, *A&A*, **689**, A134

Ma C., et al., 1998, *AJ*, **116**, 516

Malkin Z., 2016, *MNRAS*, **461**, 1937

Park R. S., Folkner W. M., Williams J. G., Boggs D. H., 2021, *AJ*, **161**, 105

Petrov L. Y., Kovalev Y. Y., 2025, *ApJS*, **276**, 38

Reid M. J., 2022, *PASP*, **134**, 123001

Rioja M. J., Dodson R., Orosz G., Imai H., Frey S., 2017, *AJ*, **153**, 105

Shepherd M. C., 1997, in Hunt G., Payne H., eds, *Astronomical Society of the Pacific Conference Series Vol. 125, Astronomical Data Analysis Software and Systems VI*. p. 77

Taylor M. B., 2005, in Shopbell P., Britton M., Ebert R., eds, *Astronomical Society of the Pacific Conference Series Vol. 347, Astronomical Data Analysis Software and Systems XIV*. p. 29

The pandas development Team 2024, pandas-dev/pandas: Pandas, doi:10.5281/zenodo.3509134

Virtanen P., et al., 2020, *Nature Methods*, **17**, 261

Wenger M., et al., 2000, *A&AS*, **143**, 9

Wilson T. L., Rohlf K., Hüttemeister S., 2013, *Tools of Radio Astronomy*, doi:10.1007/978-3-642-39950-3.

Zhang J., 2025b, FrdCHK/mcmc_ppm_estimate: First release, doi:10.5281/zenodo.15031700

Zhang J., 2025c, FrdCHK/Radio_Star_VLBI_III: Second release, doi:10.5281/zenodo.17348486

Zhang J., 2025a, FrdCHK/serial-MultiView: First release, doi:10.5281/zenodo.15030432

Zhang J., et al., 2024, *MNRAS*, **529**, 2062

Zhang J., Zhang B., Xu S., Rioja M. J., Dodson R., Mai X., Titov O., 2025a, sMV: Serial MultiView phase plane estimation, *Astrophysics Source Code Library*, record ascl:2508.016 (ascl:2508.016)

Zhang J., Zhang B., Xu S., Rioja M. J., Dodson R., Mai X., Titov O., 2025b, *AJ*, **170**, 4

Zhang J., Zhang B., Xu S., Mai X., 2025c, *A&A*, **699**, A345

APPENDIX A: VLBI IMAGES OF RADIO STARS

Here we put an example (AR Mon) of VLBI images in Fig. A1. Images of the remaining stars are available at Zenodo (Zhang 2025c).

APPENDIX B: MEASURED POSITIONS OF RADIO STARS

The successfully measured positions of all epochs of all stars are listed in Table B1.

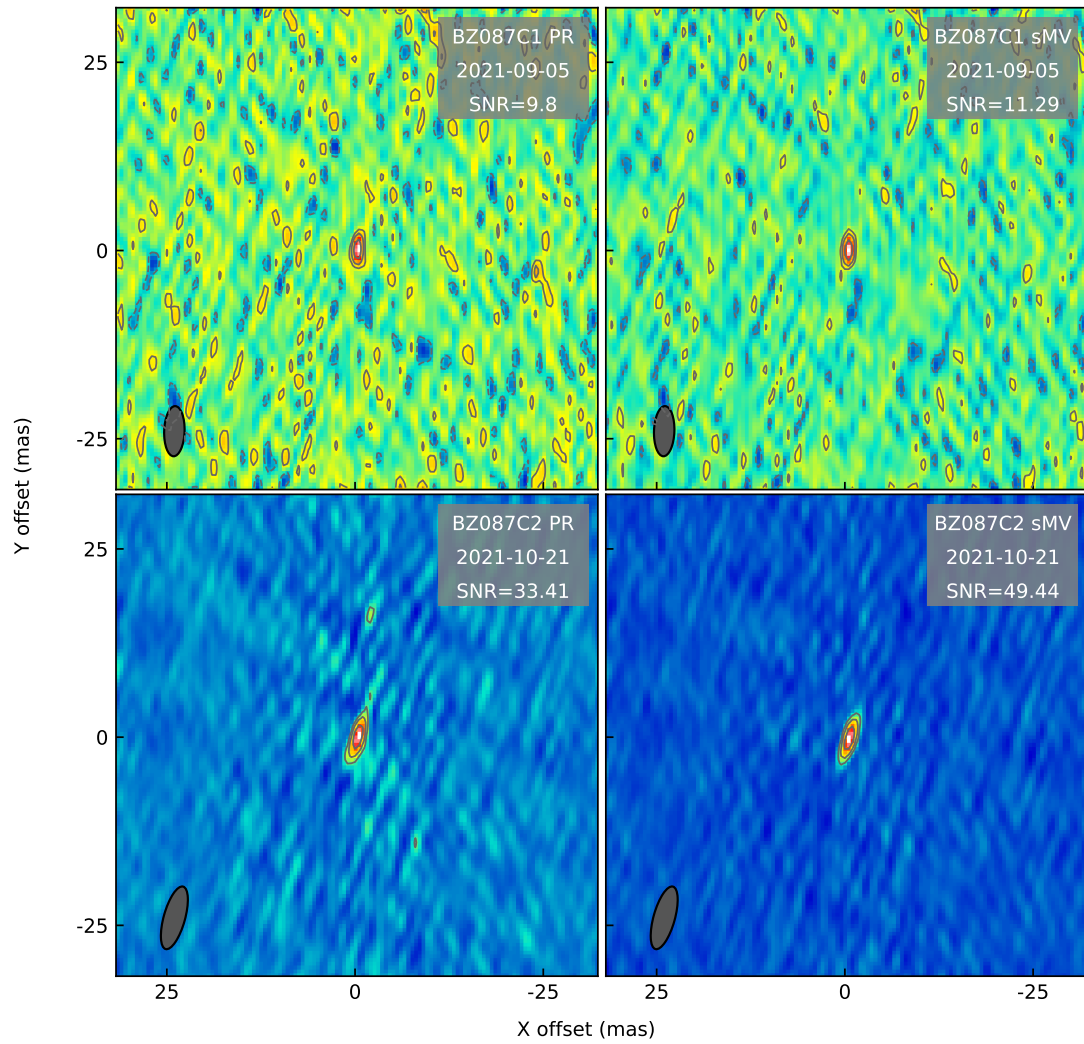


Figure A1. VLBI images of AR Mon. Left: calibrated with PR; Right: calibrated with sMV. Restored beams are shown at the bottom left corner of each panel. Contours %: -16 16 32 64. All images are cleaned with the AIPS task IMAGR.

Table B1: Measured positions of all epochs of all stars

Star	Session	Epoch	Tech.	S_{peak} (mJy Beam ⁻¹)	SNR	RA / $\Delta\alpha_*$ (^h ^m ^s) / (mas)	DEC / $\Delta\delta$ ([°] ['] ^{''}) / (mas)	σ_{α^*} (mas)	σ_{δ} (mas)
FF Aqr	BZ087A1	2021.887909	PR	1.803±0.058	31.2	22:00:36.4706982	-02:44:27.095425	0.023	0.051
			sMV	2.368±0.042	56.6	22:00:36.4707151	-02:44:27.095474	0.011	0.024
	BZ087A2	2021.986277	PR	1.958±0.094	20.8	4.486	-0.396	0.051	0.106
			sMV	2.035±0.074	27.3	4.317	-1.297	0.039	0.078
	BZ103A1	2024.421763	PR	0.657±0.033	20.1	91.181	-26.144	0.041	0.086
			sMV	0.683±0.032	21.6	91.797	-26.475	0.038	0.080
	BZ103A2	2024.451798	PR	0.527±0.041	12.9	91.773	-25.916	0.113	0.153
			sMV	0.497±0.041	12.1	92.579	-26.688	0.131	0.162
	BZ103A3	2024.503675	PR	0.586±0.040	14.7	92.568	-27.052	0.065	0.119
			sMV	0.656±0.037	17.6	93.127	-27.667	0.050	0.097
	BZ107A1	2024.915961	PR	0.711±0.046	15.3	99.308	-35.608	0.068	0.128
			sMV	0.925±0.043	21.3	99.622	-36.072	0.038	0.092
BZ107A2	2025.063430	PR	0.704±0.037	18.8	106.841	-36.825	0.032	0.081	
		sMV	0.827±0.036	22.9	106.867	-37.492	0.027	0.069	
HD 8357	BZ087A1	2021.888136	PR	0.174±0.028	6.2	01:22:56.8947396	+07:25:14.386772	0.158	0.279
			sMV	0.185±0.029	6.5	01:22:56.8947436	+07:25:14.386569	0.146	0.262
	BZ087A2	2021.986504	PR	0.269±0.047	5.7	1.711	16.232	0.148	0.307
			sMV	0.263±0.046	5.6	1.636	16.677	0.169	0.344
	BZ103A1	2024.421990	PR	0.159±0.026	6.2	268.099	595.789	0.336	0.710
			sMV	0.180±0.025	7.1	267.721	594.452	0.289	0.595
	BZ103A2	2024.452024	PR	1.267±0.104	12.2	271.346	602.984	0.193	0.391
			sMV	1.688±0.072	23.4	270.963	601.279	0.090	0.183
	BZ103A3	2024.503901	PR	0.220±0.031	7.1	279.519	615.613	0.250	0.635
			sMV	0.234±0.031	7.5	279.482	615.045	0.231	0.585
	BZ107A1	2024.916188	PR	20.036±0.822	24.4	280.829	695.850	0.039	0.075
			sMV	27.305±0.464	58.8	281.099	695.203	0.012	0.027
BZ107A2	2025.063657	PR	1.858±0.066	28.2	290.523	730.221	0.034	0.054	
		sMV	2.313±0.053	43.9	290.752	730.125	0.018	0.032	
EI Eri	BZ087B1	2021.631932	PR	2.292±0.096	23.9	04:09:40.9497982	-07:53:31.909620	0.062	0.111
			sMV	2.706±0.069	38.9	04:09:40.9498351	-07:53:31.908786	0.032	0.068
	BZ087B2	2021.694736	PR	6.912±0.173	39.9	3.006	3.141	0.023	0.051
			sMV	7.561±0.121	62.3	2.683	5.045	0.014	0.031
	BZ087B3	2022.041508	PR	13.503±0.525	25.7	-15.763	35.493	0.032	0.072
			sMV	17.904±0.324	55.2	-16.006	35.515	0.013	0.029
	BZ103B1	2024.174030	PR	1.372±0.094	14.6	58.589	280.168	0.091	0.244
			sMV	1.876±0.068	27.8	58.760	280.690	0.040	0.107
	BZ103B2	2024.255828	PR	0.529±0.035	15.0	65.091	294.059	0.070	0.167
			sMV	0.576±0.033	17.4	65.253	294.592	0.061	0.145
	BZ107B1	2024.624481	PR	3.324±0.228	14.6	109.342	336.315	0.077	0.181
			sMV	4.655±0.151	30.9	109.647	336.713	0.037	0.087
BZ107B2	2024.766461	PR	20.223±1.180	17.2	109.758	342.171	0.076	0.128	
		sMV	31.612±0.883	35.8	110.307	344.177	0.024	0.052	
V1859 Ori	BZ087B1	2021.632072	PR	3.806±0.149	25.6	05:22:54.7950173	+08:58:04.479906	0.052	0.076
			sMV	4.679±0.055	85.5	05:22:54.7949568	+08:58:04.479273	0.013	0.024
	BZ087B2	2021.694879	PR	1.265±0.033	38.2	-0.200	-1.039	0.021	0.045
			sMV	1.295±0.029	44.0	-0.444	-1.419	0.018	0.039
	BZ087B3	2022.041651	PR	0.139±0.036	3.8	-4.729	-4.677	0.405	0.550
			sMV	0.221±0.035	6.3	-5.066	-5.606	0.200	0.359
	BZ103B1	2024.174174	PR	1.188±0.066	18.0	-4.064	-25.400	0.056	0.106
			sMV	1.581±0.046	34.4	-4.522	-25.226	0.030	0.058
	BZ103B2	2024.255971	PR	0.555±0.035	15.7	-3.663	-25.689	0.058	0.103
			sMV	0.676±0.031	21.6	-4.076	-25.745	0.035	0.069
	BZ107B1	2024.624624	PR	1.260±0.070	18.0	2.951	-27.188	0.055	0.162
			sMV	1.753±0.052	33.7	2.834	-28.645	0.027	0.072
BZ107B2	2024.766604	PR	0.347±0.033	10.4	3.394	-30.231	0.071	0.197	
		sMV	0.447±0.033	13.6	3.294	-30.444	0.051	0.126	

Table B1: continued

Star	Session	Epoch	Tech.	S_{peak} (mJy Beam ⁻¹)	SNR	RA / $\Delta\alpha_*$ (^h ^m ^s) / (mas)	DEC / $\Delta\delta$ ([°] ['] ^{''}) / (mas)	σ_{α^*} (mas)	σ_{δ} (mas)
V1355 Ori	BZ087C2	2021.804178	PR	1.224±0.034	35.6	06:02:40.3781456	-00:51:36.971648	0.022	0.046
			sMV	1.245±0.033	37.5	06:02:40.3781582	-00:51:36.971629	0.021	0.044
	BZ103C1	2024.166067	PR	4.894±0.136	35.9	15.153	27.843	0.027	0.063
			sMV	5.301±0.084	62.9	15.192	27.492	0.016	0.039
	BZ103C2	2024.236962	PR	1.190±0.041	29.2	15.405	29.910	0.032	0.078
			sMV	1.254±0.033	38.2	15.730	29.822	0.025	0.061
	BZ103C3	2024.340697	PR	0.896±0.040	22.2	18.907	32.939	0.038	0.076
			sMV	0.959±0.037	25.6	19.202	32.624	0.033	0.065
	BZ107C1	2024.706567	PR	0.399±0.030	13.4	37.170	35.209	0.047	0.106
			sMV	0.426±0.029	14.9	37.482	34.889	0.039	0.093
BZ107C2	2024.829434	PR	1.834±0.067	27.3	37.095	34.569	0.025	0.058	
		sMV	2.275±0.041	55.4	37.320	34.230	0.011	0.025	
AR Mon	BZ087C1	2021.678721	PR	0.276±0.028	9.8	07:20:48.4647689	-05:15:35.943597	0.054	0.142
			sMV	0.311±0.028	11.3	07:20:48.4647784	-05:15:35.943515	0.049	0.125
	BZ087C2	2021.804318	PR	1.503±0.045	33.4	1.002	-1.852	0.022	0.055
			sMV	1.657±0.034	49.4	1.253	-1.711	0.015	0.036
XY UMa	BZ087D1	2021.771742	PR	0.212±0.031	6.8	09:09:55.8125729	+54:29:13.740698	0.133	0.158
			sMV	0.291±0.036	8.2	09:09:55.8125171	+54:29:13.740163	0.133	0.138
	BZ087D2	2021.930104	PR	0.474±0.035	13.7	-8.208	-20.022	0.107	0.112
			sMV	0.474±0.035	13.6	-8.784	-20.595	0.109	0.111
	BZ103D2	2024.343721	PR	0.187±0.033	5.6	-154.854	-459.799	0.333	0.520
			sMV	0.229±0.034	6.7	-155.240	-460.258	0.257	0.376
FF UMa	BZ087D1	2021.771867	PR	1.583±0.044	35.8	09:33:46.4844440	+62:49:39.766235	0.040	0.047
			sMV	1.687±0.041	41.1	09:33:46.4844371	+62:49:39.766465	0.034	0.039
	BZ087D2	2021.930229	PR	1.932±0.045	43.0	-2.276	1.769	0.051	0.033
			sMV	2.163±0.039	55.0	-2.334	2.169	0.036	0.025
	BZ103D1	2024.283813	PR	7.684±0.131	58.5	-63.833	-46.719	0.024	0.019
			sMV	8.039±0.105	76.6	-63.878	-46.306	0.018	0.014
	BZ103D2	2024.343846	PR	1.244±0.052	24.1	-66.210	-49.814	0.086	0.060
			sMV	1.363±0.049	28.0	-66.241	-49.301	0.071	0.048
	BZ103D3	2024.425792	PR	2.138±0.035	60.6	-67.384	-54.893	0.028	0.021
			sMV	2.186±0.034	65.3	-67.572	-54.408	0.026	0.019
	BZ107D1	2024.797123	PR	18.223±0.317	57.4	-59.918	-66.789	0.037	0.020
			sMV	20.479±0.235	87.1	-59.882	-66.397	0.022	0.013
	BZ107D2	2024.933642	PR	0.692±0.035	19.6	-62.808	-64.809	0.142	0.073
			sMV	0.782±0.034	22.8	-62.874	-64.115	0.110	0.060
DM UMa	BZ087D1	2021.771984	PR	0.576±0.035	16.5	10:55:43.4325037	+60:28:09.551923	0.080	0.085
			sMV	0.389±0.037	10.6	10:55:43.4323585	+60:28:09.548613	0.155	0.146
	BZ087D2	2021.930345	PR	0.688±0.042	16.5	-3.660	1.788	0.087	0.091
			sMV	0.581±0.045	12.9	-4.342	0.386	0.111	0.123
	BZ103D1	2024.283929	PR	0.566±0.043	13.3	-101.085	-10.588	0.119	0.088
			sMV	0.499±0.044	11.2	-101.562	-11.738	0.135	0.110
	BZ103D2	2024.343962	PR	1.801±0.069	26.2	-104.653	-12.142	0.077	0.060
			sMV	1.057±0.102	10.4	-105.393	-13.113	0.205	0.163
	BZ103D3	2024.425909	PR	0.318±0.031	10.3	-108.324	-14.821	0.209	0.142
			sMV	0.251±0.032	7.7	-108.794	-16.031	0.248	0.215
	BZ107D1	2024.797240	PR	0.803±0.054	14.9	-113.988	-22.986	0.184	0.099
			sMV	0.719±0.060	12.0	-114.694	-24.479	0.213	0.133

Table B1: continued

Star	Session	Epoch	Tech.	S_{peak} (mJy Beam ⁻¹)	SNR	RA / $\Delta\alpha_*$ (^h ^m ^s) / (mas)	DEC / $\Delta\delta$ ([°] ['] ^{''}) / (mas)	σ_{α^*} (mas)	σ_{δ} (mas)
RS CVn	BZ087E1	2021.608702	PR	3.569±0.066	54.1	13:10:36.8185054	+35:56:06.032171	0.026	0.025
			sMV	3.575±0.068	52.8	13:10:36.8185116	+35:56:06.031949	0.027	0.026
	BZ087E2	2021.630576	PR	2.407±0.074	32.3	-0.601	0.416	0.064	0.044
			sMV	2.480±0.072	34.7	-0.803	0.131	0.059	0.041
	BZ103E1	2024.107030	PR	0.734±0.036	20.4	-112.861	52.828	0.071	0.064
			sMV	0.737±0.036	20.6	-112.963	52.908	0.070	0.063
	BZ103E2	2024.197093	PR	0.870±0.037	23.7	-120.131	57.650	0.079	0.070
			sMV	0.877±0.037	23.9	-120.259	57.767	0.078	0.069
	BZ107E1	2024.633992	PR	0.423±0.035	12.2	-150.792	61.924	0.158	0.099
			sMV	0.428±0.035	12.4	-150.844	61.798	0.155	0.097
	BZ107E2	2024.680392	PR	1.463±0.049	29.6	-151.395	61.470	0.064	0.041
			sMV	1.450±0.050	28.9	-151.505	61.414	0.068	0.043
RS UMi	BZ087E1	2021.608417	PR	0.303±0.033	9.2	15:50:49.4485186	+72:12:40.443268	0.345	0.177
			sMV	0.197±0.034	5.8	15:50:49.4483801	+72:12:40.443232	0.578	0.264
	BZ087E3	2021.949714	PR	0.514±0.035	14.5	4.062	-5.358	0.227	0.097
			sMV	0.520±0.035	14.7	3.354	-4.780	0.222	0.095
	BZ103E2	2024.196808	PR	1.031±0.048	21.3	12.644	-21.885	0.144	0.077
			sMV	1.197±0.042	28.8	12.044	-21.153	0.111	0.049
	BZ107E1	2024.633709	PR	1.921±0.047	41.0	9.827	-26.122	0.073	0.037
			sMV	1.677±0.041	41.3	9.399	-26.698	0.076	0.039
	BZ107E2	2024.680108	PR	2.029±0.043	46.6	10.209	-26.927	0.059	0.032
			sMV	1.373±0.043	32.2	9.583	-27.193	0.094	0.053

All results are produced by the AIPS task JMFIT. Column ‘‘Tech.’’ denotes calibration technique, PR or sMV. S_{peak} denotes peak flux density, and SNR denotes signal-to-noise ratio in image. The coordinates in the first two rows of each star are taken as reference positions for PR and sMV, respectively, and the offsets in other rows are relative to them.

APPENDIX C: ESTIMATED PARALLAX CURVES OF RADIO STARS

The estimated parallax curves for ten stars are presented here, calibrated using both PR and sMV.

APPENDIX D: CORRELATION COEFFICIENT MATRICES OF ADOPTED ASTROMETRIC SOLUTIONS

The correlation coefficients among the astrometric parameters, $\text{corr}[\alpha, \delta, \varpi, \mu_\alpha, \mu_\delta]$ (RA, DEC, parallax, and proper motions in the RA and DEC directions), are listed below. In general, the most significant correlations occur between α and μ_α , and between δ and μ_δ , which is physically expected given the coupling between source position and linear proper motion. A relatively high correlation is also present between ϖ and the two RA-direction parameters (α and μ_α), because we were primarily sampling at the extremes of parallax sinusoids projected onto the RA direction, as shown in Appendix C. The remaining terms in the correlation coefficient matrices are relatively small.

FF Aqr

$$\text{corr}[\alpha, \delta, \varpi, \mu_\alpha, \mu_\delta] = \begin{bmatrix} +1.000 & +0.059 & +0.378 & -0.511 & -0.085 \\ \dots & +1.000 & +0.112 & -0.052 & -0.413 \\ \dots & \dots & +1.000 & -0.425 & -0.138 \\ \dots & \dots & \dots & +1.000 & +0.063 \\ \dots & \dots & \dots & \dots & +1.000 \end{bmatrix} \quad (\text{D1})$$

HD 8357

$$\text{corr}[\alpha, \delta, \varpi, \mu_\alpha, \mu_\delta] = \begin{bmatrix} +1.000 & +0.012 & +0.214 & -0.509 & -0.000 \\ \dots & +1.000 & +0.032 & -0.014 & -0.466 \\ \dots & \dots & +1.000 & -0.318 & -0.054 \\ \dots & \dots & \dots & +1.000 & -0.008 \\ \dots & \dots & \dots & \dots & +1.000 \end{bmatrix} \quad (\text{D2})$$

EI Eri

$$\text{corr}[\alpha, \delta, \varpi, \mu_\alpha, \mu_\delta] = \begin{bmatrix} +1.000 & -0.008 & -0.246 & -0.114 & +0.043 \\ \dots & +1.000 & +0.042 & +0.001 & -0.061 \\ \dots & \dots & +1.000 & +0.190 & -0.023 \\ \dots & \dots & \dots & +1.000 & +0.006 \\ \dots & \dots & \dots & \dots & +1.000 \end{bmatrix} \quad (\text{D3})$$

VI859 Ori

$$\text{corr}[\alpha, \delta, \varpi, \mu_\alpha, \mu_\delta] = \begin{bmatrix} +1.000 & +0.041 & -0.319 & -0.204 & -0.035 \\ \dots & +1.000 & -0.111 & -0.038 & +0.033 \\ \dots & \dots & +1.000 & +0.272 & +0.065 \\ \dots & \dots & \dots & +1.000 & -0.003 \\ \dots & \dots & \dots & \dots & +1.000 \end{bmatrix} \quad (\text{D4})$$

VI355 Ori

$$\text{corr}[\alpha, \delta, \varpi, \mu_\alpha, \mu_\delta] = \begin{bmatrix} +1.000 & -0.041 & -0.087 & -0.570 & +0.041 \\ \dots & +1.000 & +0.042 & +0.015 & -0.592 \\ \dots & \dots & +1.000 & +0.205 & -0.030 \\ \dots & \dots & \dots & +1.000 & -0.020 \\ \dots & \dots & \dots & \dots & +1.000 \end{bmatrix} \quad (\text{D5})$$

XY UMa

Since XY UMa was only detected in three epochs, the correlation coefficients between astrometric parameters are extremely high.

$$\text{corr}[\alpha, \delta, \varpi, \mu_\alpha, \mu_\delta] = \begin{bmatrix} +1.000 & -0.107 & +0.492 & +0.683 & -0.187 \\ \dots & +1.000 & -0.226 & -0.218 & +0.917 \\ \dots & \dots & +1.000 & +0.957 & -0.384 \\ \dots & \dots & \dots & +1.000 & -0.369 \\ \dots & \dots & \dots & \dots & +1.000 \end{bmatrix} \quad (\text{D6})$$

FF UMa

$$\text{corr}[\alpha, \delta, \varpi, \mu_\alpha, \mu_\delta] = \begin{bmatrix} +1.000 & -0.019 & -0.227 & -0.440 & -0.035 \\ \dots & +1.000 & +0.078 & +0.014 & -0.384 \\ \dots & \dots & +1.000 & +0.385 & -0.123 \\ \dots & \dots & \dots & +1.000 & -0.025 \\ \dots & \dots & \dots & \dots & +1.000 \end{bmatrix} \quad (\text{D7})$$

DM UMa

$$\text{corr}[\alpha, \delta, \varpi, \mu_\alpha, \mu_\delta] = \begin{bmatrix} +1.000 & +0.014 & -0.077 & -0.144 & -0.013 \\ \dots & +1.000 & +0.069 & +0.046 & -0.255 \\ \dots & \dots & +1.000 & +0.616 & -0.271 \\ \dots & \dots & \dots & +1.000 & -0.152 \\ \dots & \dots & \dots & \dots & +1.000 \end{bmatrix} \quad (\text{D8})$$

RS CVn

$$\text{corr}[\alpha, \delta, \varpi, \mu_\alpha, \mu_\delta] = \begin{bmatrix} +1.000 & -0.004 & +0.466 & -0.293 & +0.004 \\ \dots & +1.000 & +0.015 & +0.005 & -0.151 \\ \dots & \dots & +1.000 & -0.539 & -0.030 \\ \dots & \dots & \dots & +1.000 & +0.024 \\ \dots & \dots & \dots & \dots & +1.000 \end{bmatrix} \quad (\text{D9})$$

RS UMi

$$\text{corr}[\alpha, \delta, \varpi, \mu_\alpha, \mu_\delta] = \begin{bmatrix} +1.000 & -0.033 & -0.080 & -0.813 & +0.007 \\ \dots & +1.000 & +0.066 & +0.052 & -0.208 \\ \dots & \dots & +1.000 & +0.460 & -0.008 \\ \dots & \dots & \dots & +1.000 & -0.017 \\ \dots & \dots & \dots & \dots & +1.000 \end{bmatrix} \quad (\text{D10})$$

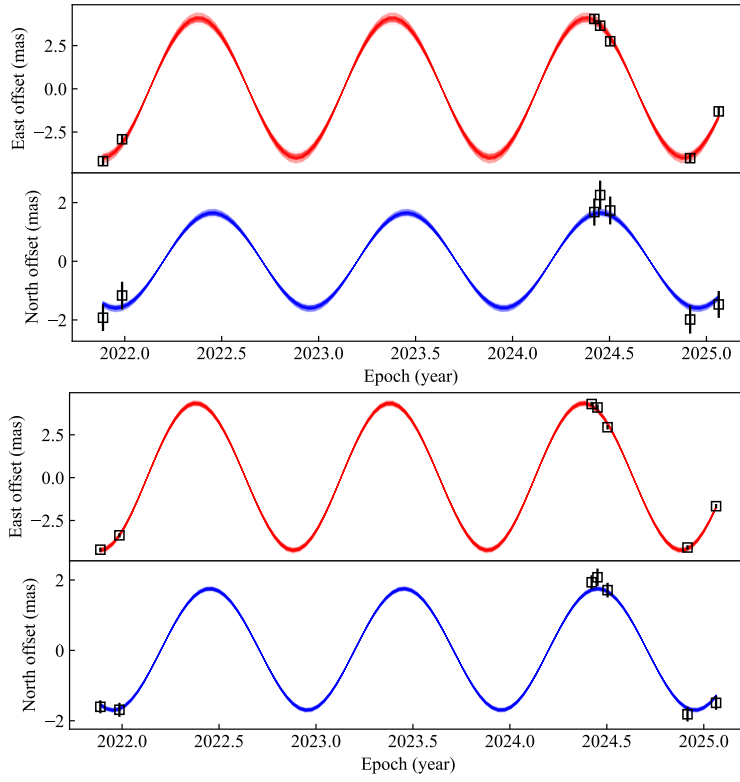


Figure C1. Estimated parallax curves of FF Aqr. Upper panel: calibrated with PR; Lower panel: calibrated with sMV. The broadening of the curves represents the probability distribution of estimated astrometric parameters.

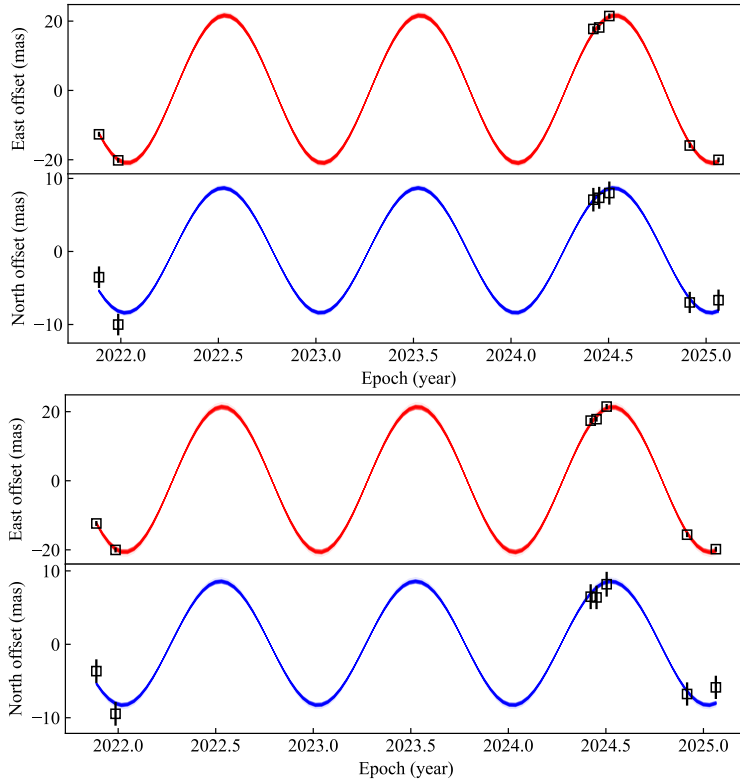


Figure C2. Estimated parallax curves of HD 8357. All elements in the figure are kept the same as Fig. C1.

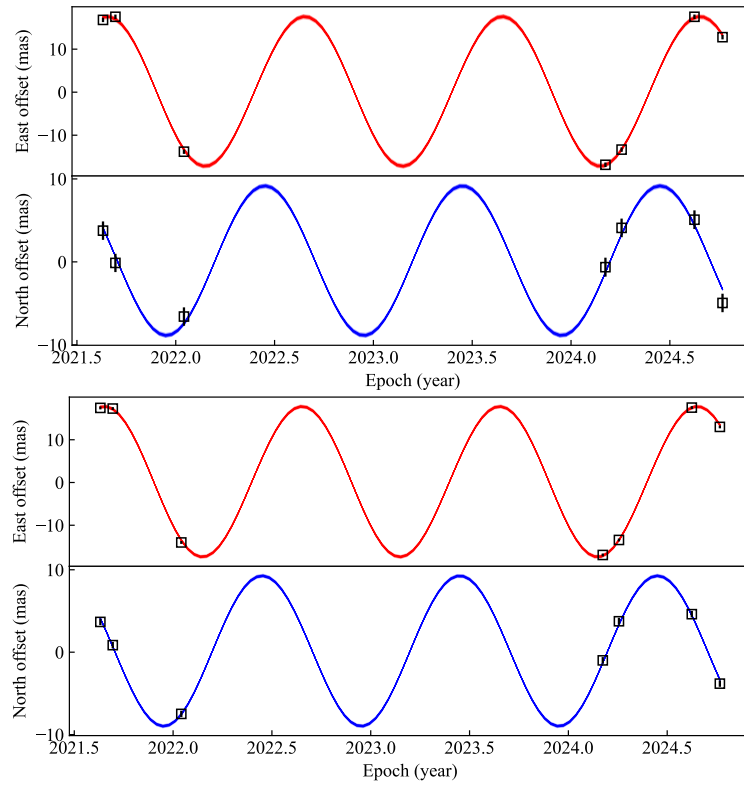


Figure C3. Estimated parallax curves of EI Eri. All elements in the figure are kept the same as Fig. C1.

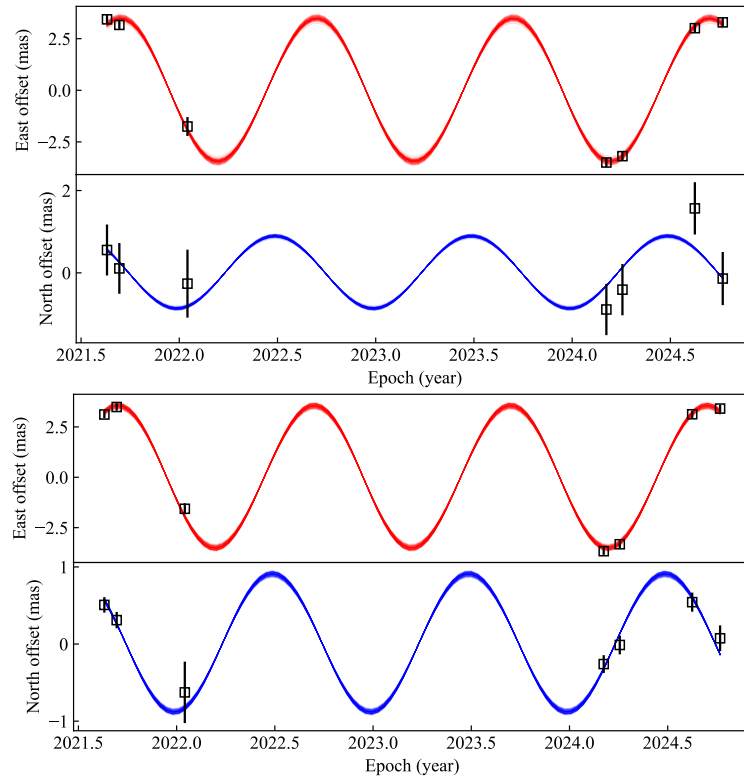


Figure C4. Estimated parallax curves of V1859 Ori. All elements in the figure are kept the same as Fig. C1.

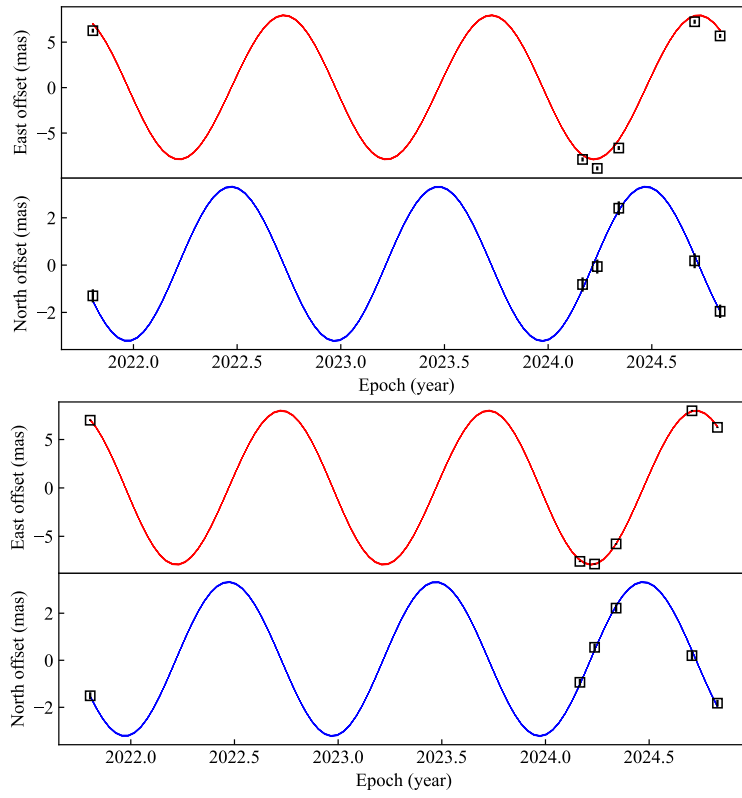


Figure C5. Estimated parallax curves of V1355 Ori. All elements in the figure are kept the same as Fig. C1.

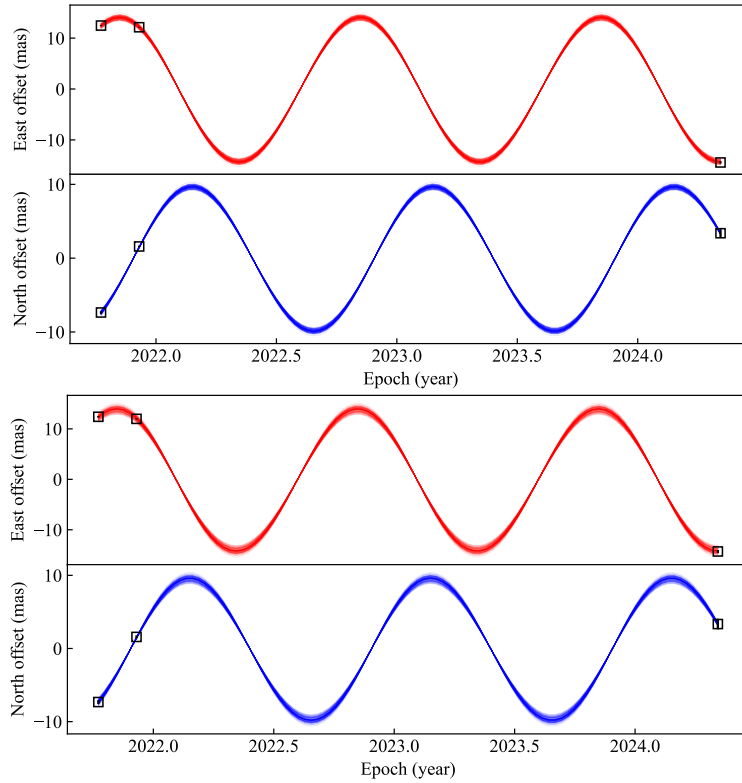


Figure C6. Estimated parallax curves of XY UMa. All elements in the figure are kept the same as Fig. C1.

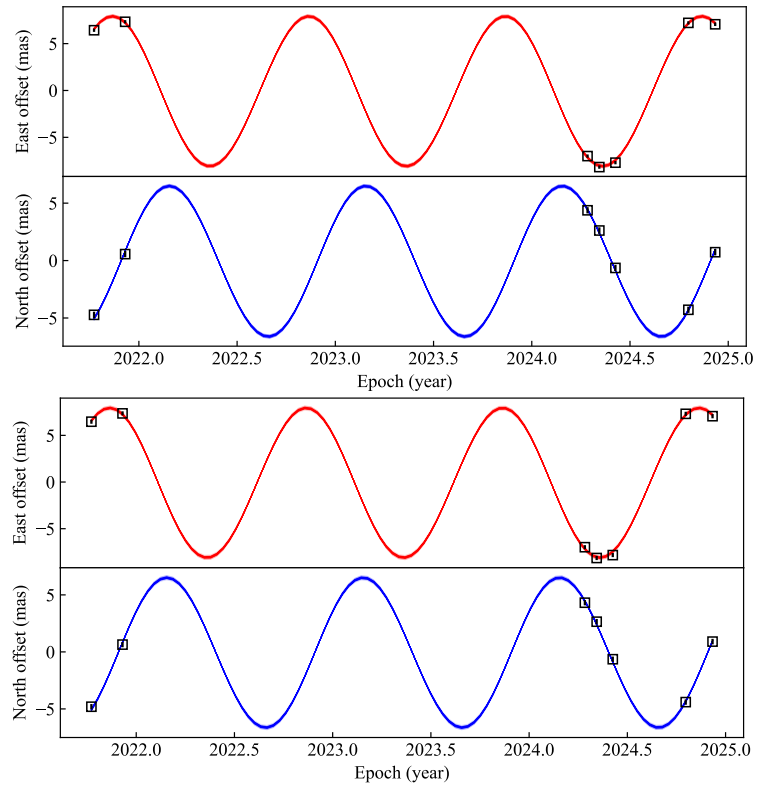


Figure C7. Estimated parallax curves of FF UMa. All elements in the figure are kept the same as Fig. C1.

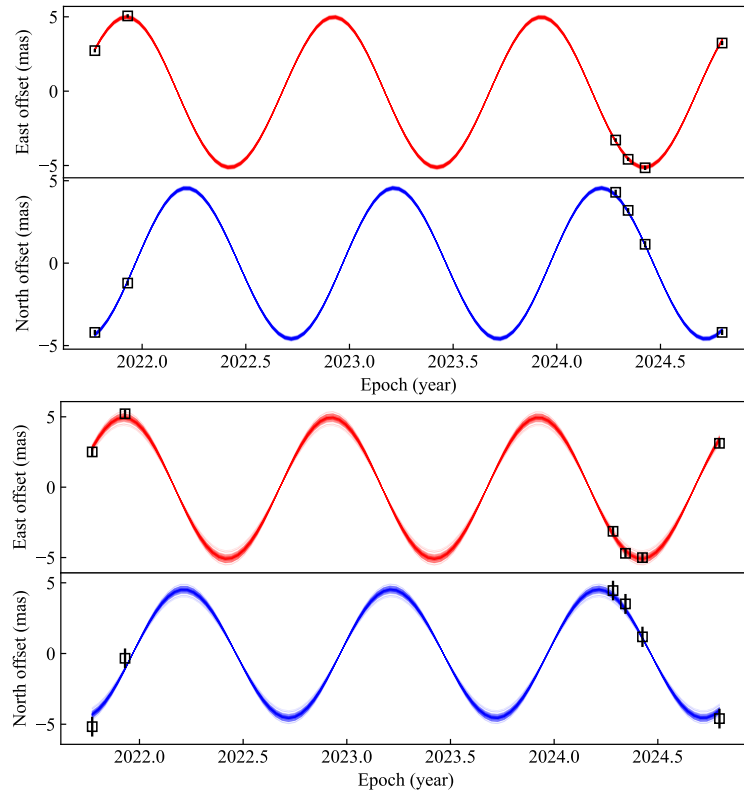


Figure C8. Estimated parallax curves of DM UMa. All elements in the figure are kept the same as Fig. C1.

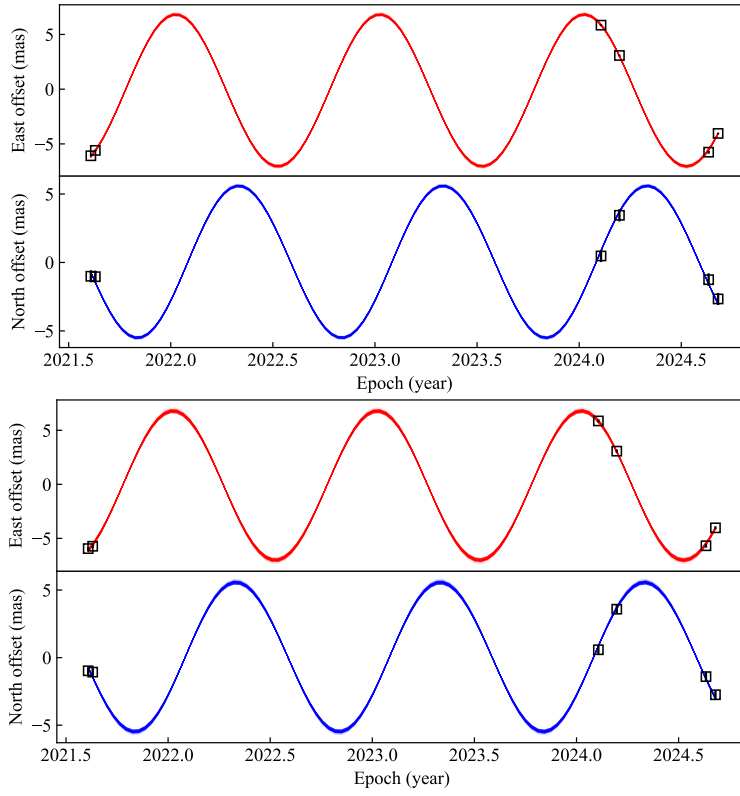


Figure C9. Estimated parallax curves of RS CVn. All elements in the figure are kept the same as Fig. C1.

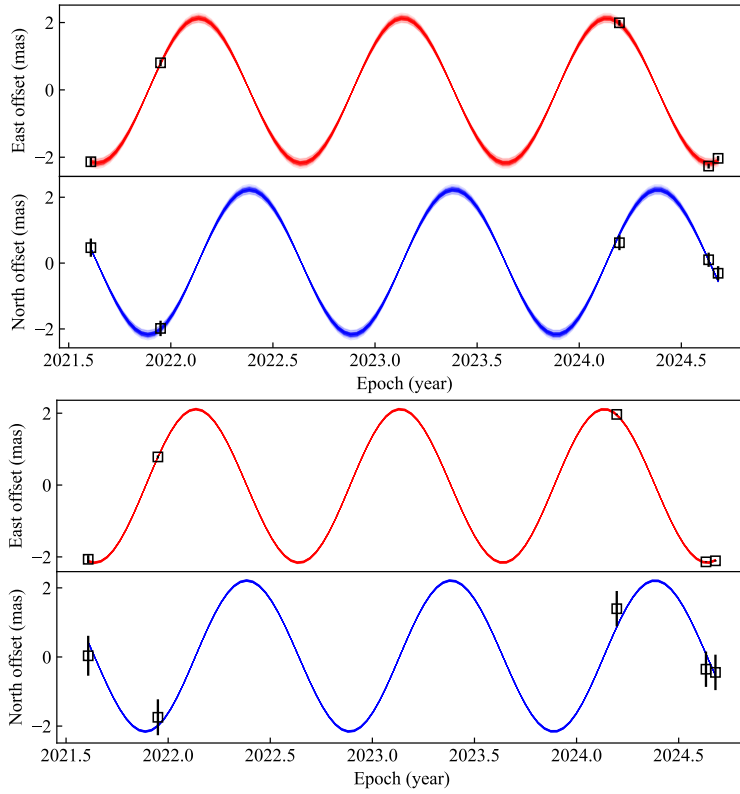


Figure C10. Estimated parallax curves of RS UMi. All elements in the figure are kept the same as Fig. C1.

APPENDIX E: SELF-CALIBRATED IMAGES OF CALIBRATORS

We present self-calibrated images of calibrators that have significant source structures here. Epochs in which all ten VLBA antennas participated are selected for the best UV coverage. Note that each image has a different field of view (FOV). The cleaning and self-calibration are done using Difmap ([Shepherd 1997](#)).

This paper has been typeset from a \TeX/L\AA\TeX file prepared by the author.

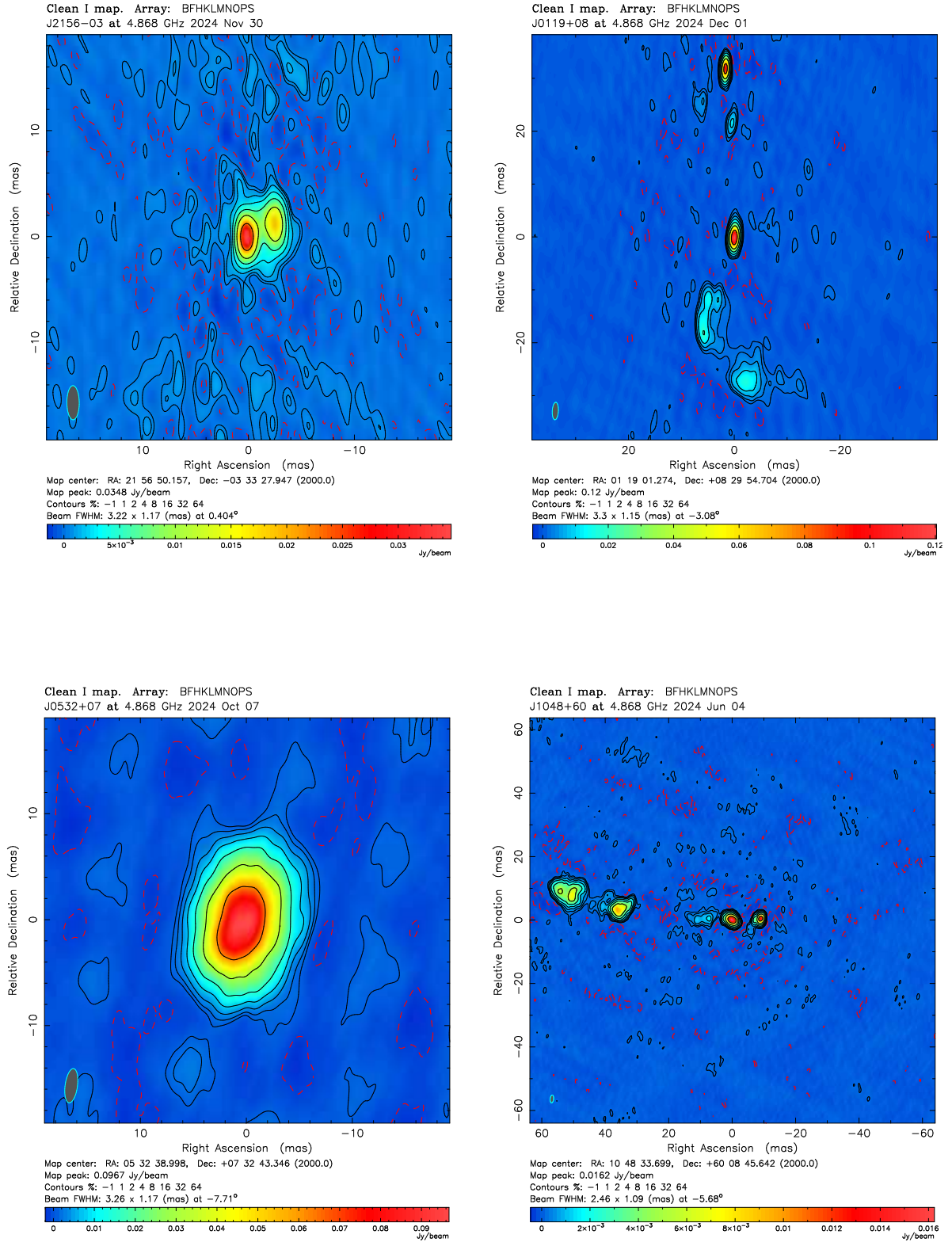


Figure E1. Self-calibrated images of: J2156-0333 (upper left); J0119+0829 (upper right); J0532+0732 (lower left); J1048+6008 (lower right).

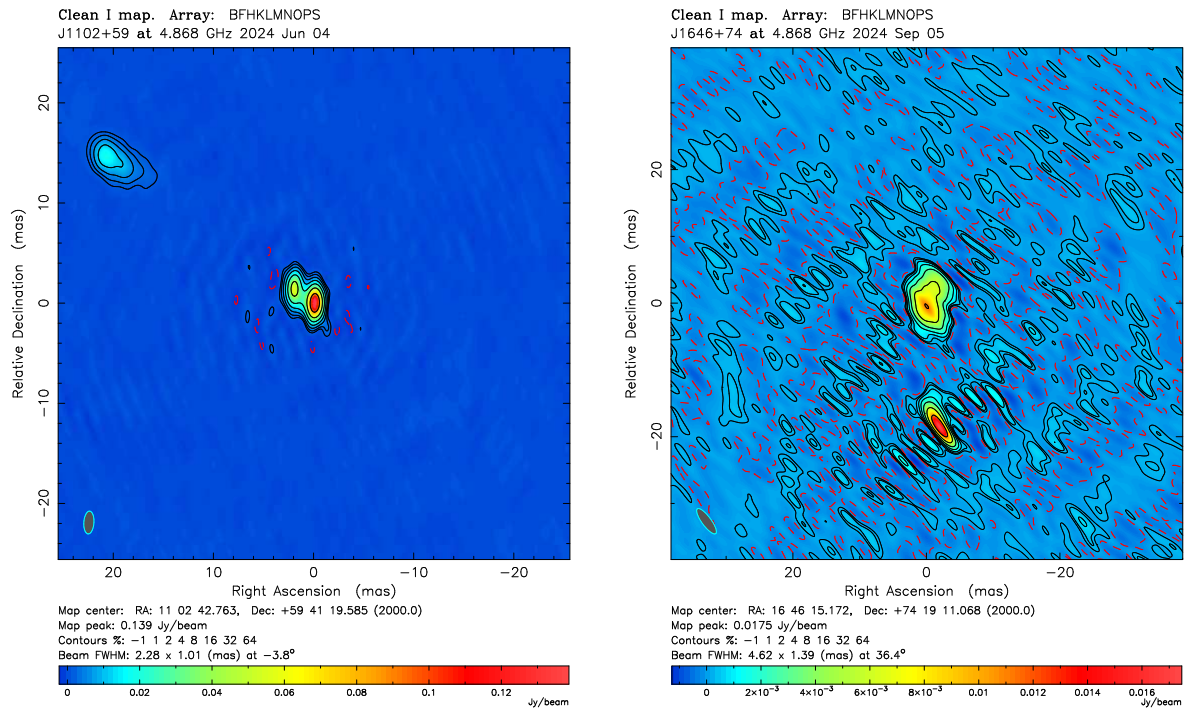


Figure E2. Self-calibrated images of: J1102+5941 (left); J1646+7419 (right).